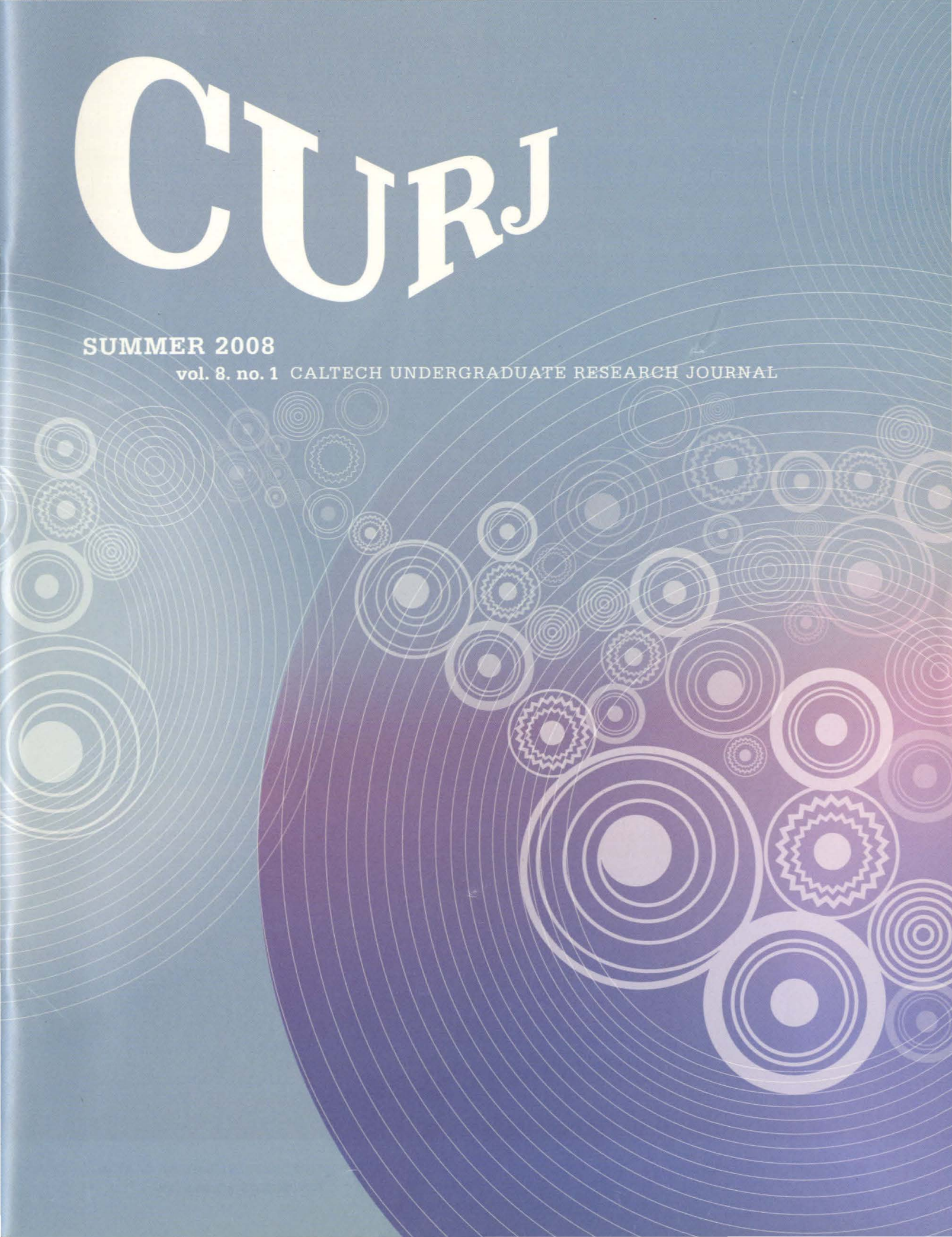


CURJ

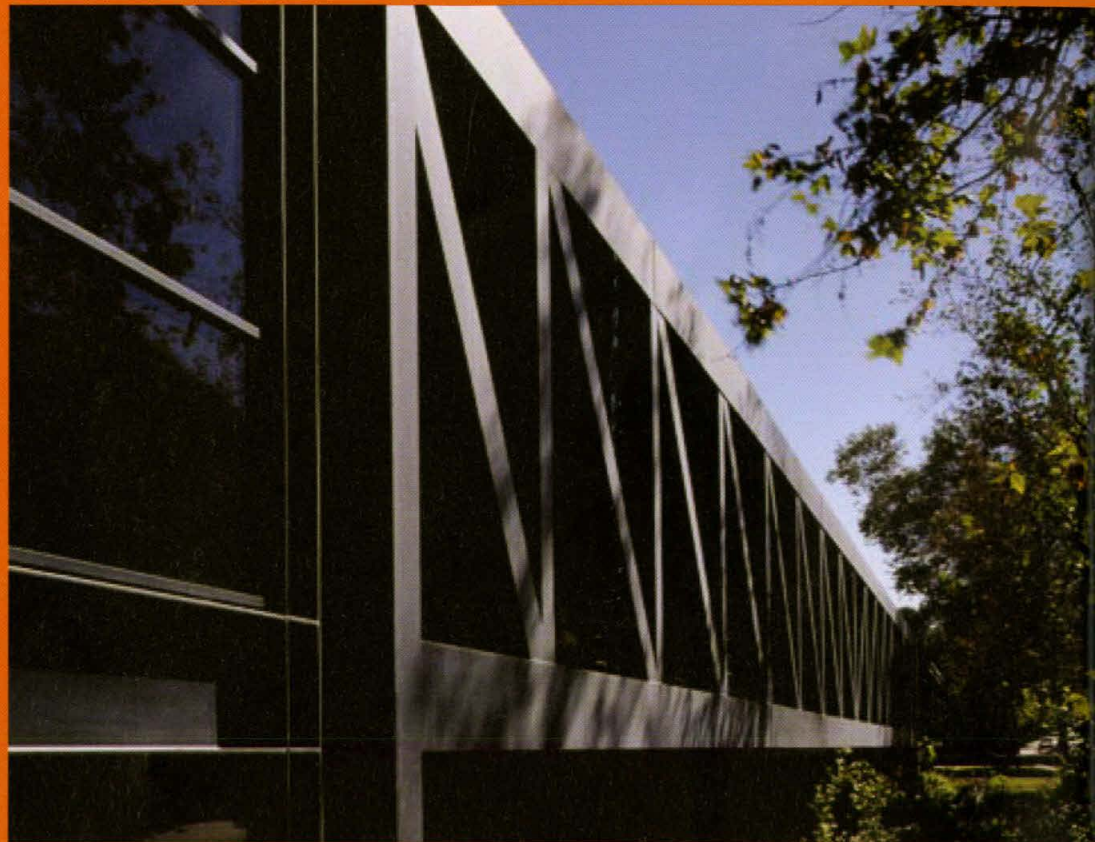
SUMMER 2008

vol. 8. no. 1 CALTECH UNDERGRADUATE RESEARCH JOURNAL



Art Center College of Design

One of the world's preeminent art and design colleges, Art Center College of Design is renowned for its culture of innovation, rigorous transdisciplinary curriculum, superb professional faculty and extensive relationships with industry. For 80 years, Art Center has prepared an influential group of artists and designers to become leaders both in their chosen fields and the world at large.



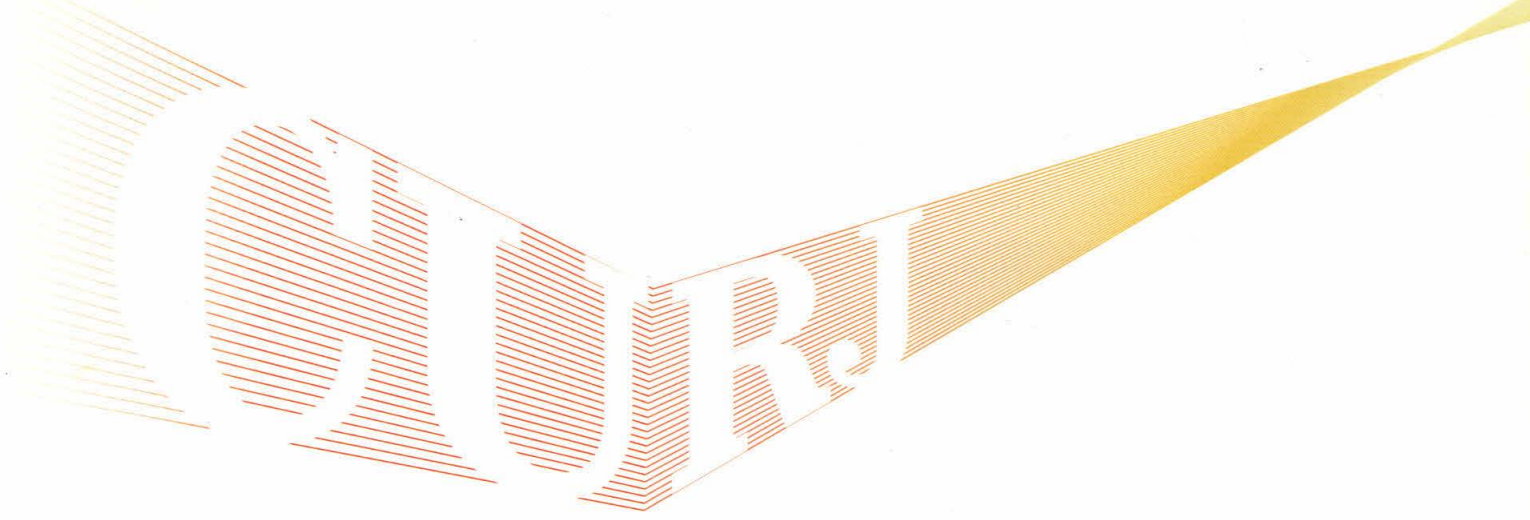
UNDERGRADUATE PROGRAMS

Advertising
Entertainment Design
Environmental Design
Film
Fine Art
Graphic Design
Illustration
Photography and Imaging
Product Design
Transportation Design

GRADUATE PROGRAMS

Art
Broadcast Cinema
Industrial Design
Media Design

CURJ IS A COLLABORATIVE EFFORT BY STUDENTS AT ART CENTER COLLEGE OF DESIGN AND THE CALIFORNIA INSTITUTE OF TECHNOLOGY.

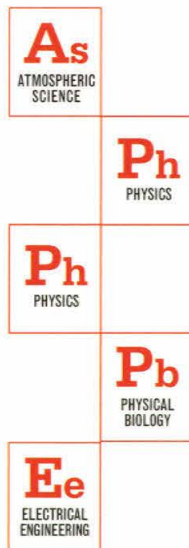


Interview

- 6 **President Jean-Lou Chameau, Eighth President of the California Institute of Technology**
by Harish Vasudevan

Research

- 8 **Searching for Evidence of Planet Formation in p Ophiuchus—Applying a Period-Searching Algorithm to Near-Infrared Time-Series Photometry**
By Alan H. Gee & Peter Plavchan
- 18 **Making Sure Advanced Ligo will be Clean Enough to Hear the Big Bang**
by Edward Macaulay
- 28 **High-Order Surface Modeling: Automatic Design of Projection Surfaces**
by Brandt A Belson
- 36 **Ultrafast Electron Microscopy: Watching Atoms Move and Crystals Melt**
By Garrett K. Drayna & David J. Flannigan (Ph.D)
- 44 **Wireless Power in Space**
By Will Biederman, Yoseph Bar-Cohen, Xiaoqi Bao, Stewart Sherrit, Mircea Badescu & Chris Jones



THE CALTECH UNDER-
GRADUATE RESEARCH
JOURNAL INVITES
REVIEW & RESEARCH
SUBMISSIONS
FROM UNDERGRADUATES
AT ANY INSTITUTION.

CURJ

for more information:
www.curj.caltech.edu

SURF

PROGRAM

Caltech's **Summer Undergraduate Research Fellowships** program introduces students to research under the guidance of seasoned mentors.

Students experience the process of research as a creative intellectual activity and gain a more realistic view of the opportunities and demands of a professional research career.

Fellowships are also available to non-Caltech students.

For more information go to
<http://surf.caltech.edu>
or phone 626.395.2885

EXECUTIVE EDITORS*Editor-in-Chief*

Harish Vasudevan

Executive Content Editors

Simon Kung

Angela Shih

Art Director / Designer

Eun Joo Annie Kim

Executive Online Editor

Kelly Littlepage

Executive Operations Manager

Pradeep Bugga

ASSOCIATE CONTENT EDITORS

Csilla Felsen

Andrew Freddo

Han Bin Man

Joy Sheng

STAFF COLLABORATORS

Nils Lindstrom

Graphics Advisor, Art Center College of Design

Candace Rypisi

Director, Student Faculty Programs

Steven Youra

Director, Hixon Writing Center

CURJ DONORS

Caltech Administration

Typecraft, Inc

**CALTECH UNDERGRADUATE
RESEARCH JOURNAL** vol. 8. no. 1

● Art Center College of Design

from the editor

As our society advances, scientific knowledge, based on findings from the lab, plays an increasingly large role in everyday life. The work of past researchers is embedded into many of our daily routines — in actions as basic as taking a decongestant to relieve cold symptoms or using the Internet to check the latest news. However, most people take these small wonders for granted and hardly consider the scientists responsible for making them happen. How many of us can explain why decongestants help us breathe freely or how information we send over the Internet is encoded and transmitted? Further, how many people can name the important thinkers responsible for these minor miracles? Since we don't need to understand these intricacies for them to be effective, we often choose not to. And understandably so, as learning how these things work and who figured them out takes time and effort away from our busy daily routines. But perhaps we should all take the time and effort to simply appreciate how truly amazing these everyday accomplishments are.

Because these accomplishments are amazing. As are the people responsible for them. The Caltech Undergraduate Research Journal honors these incredible researchers and their accomplishments by providing an avenue for some of the most innovative, young scientific minds in the country to present their work. Undergraduates can and do conduct meaningful research, and by understanding this research, scientists of all ages and abilities can take pride in the incredible success that the science leaders of tomorrow are achieving today.

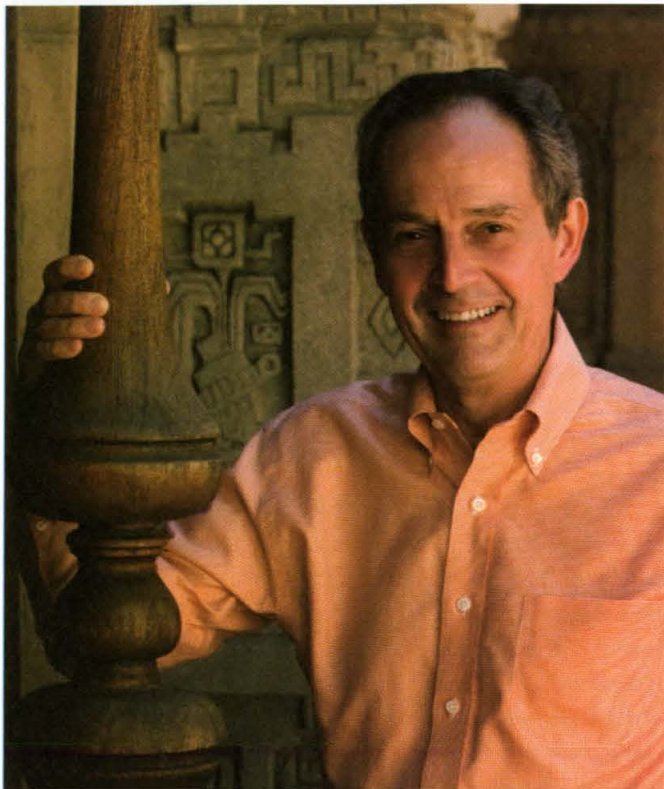
With these sentiments, we proudly share with readers the work of a few budding researchers working on a diverse range of projects. Our hope is that, by understanding the accomplishments of these undergraduate researchers, we can reflect on the intellectual aptitude and genuine hard work required for innovation.

Best Wishes,

Harish Vasudevan
Editor-in-Chief

Interview with the professor Jean-Lou Chameau Eighth President of the California Institute of Technology.

by Harish Vasudevan



HV — How did you first become interested in coming to Caltech? What special qualities attracted you here as opposed to other career opportunities?

JLC — I actually wasn't even aware that Caltech had an opening for the position of President! The Caltech Search Committee contacted me, and one discussion led to another. Obviously, it was very attractive, and the reason for this was because of the students and faculty. In life, when you have the opportunity to work with great people, you take it. I think this is true for any job you have: the people are the key. Having the opportunity to start working with such outstanding people in a great organization was extremely attractive.

You clearly have a very distinguished research career. How did you end up switching away from research and toward more of an administrative and leadership role?

Totally by accident. When I was doing my research as an academic professor, I was doing quite well and was very pleased with the way things were going. Plus, I loved the teaching aspect. At the time, I had no intention or interest in getting involved with administration, and I had no idea what administrators did anyway.

However, I "stumbled" into an academic administrative role when I was a faculty member at Purdue University. I was working with a very distinguished group of colleagues; however, they could not get along very well. The Chair of the department told me that "the only thing they agree on is they like working with you," and he proceeded to ask that I organize the collaborations. I agreed, and then one thing led to another. I then realized, over a number of years, that I really enjoyed working with people and developing new programs; in short, I loved the leadership aspects of my job. It became as rewarding as my own research.

What are some of the differences between your job as a researcher and as President?

The biggest difference is that when you are doing your own research, you focus on one topic. You might have several projects going on at a given time, but you are still focused on one area of interest. As a President or Chair or Dean, your time is spent on large number of different issues, all of

» My advice is to do what excites you. Whatever you do, you must do it with passion «

which are very different in nature. You no longer have the luxury of focusing on any one thing. This makes time management even more critical in a leadership position.

Another crucial contrast are the different rewards you get from research and as a leader. In research, you get credit for your own accomplishments. Results are attributed directly to you. In leadership, your rewards come from the accomplishments of others and knowing you played a small role in those accomplishments.

You have always been a proponent for interdisciplinary studies and building collaborations between different groups of people. How can we, as undergraduates, incorporate this into our scientific education?

In a way, it's built into the undergraduate education at Caltech. For example, if you major in mechanical engineering or biology, you only take a percentage of your classes in a particular discipline. Thus, you take courses and gain experience in a broad number of disciplines encompassing both science and the humanities. While you do not become an expert in any one discipline, you get a flavor for each and go in depth enough to understand what those disciplines are about. This forms a good foundation for a variety of sciences.

As far as how you can integrate these disciplines, it's hard to do, and I'm not sure how well it's done in education. This is a bit of what you get from research. You get a feel for how things can be mixed together. I'm not sure that this integration can be fully taught. Rather, it's something you learn by doing.

You seem to be very involved in undergraduate life at Caltech. What do you feel makes Caltech undergraduates unique?

The undergrads here are quite fun. They're smart, a bit eccentric, and organize lots of fun activities. The Caltech undergraduate experience is a fascinating opportunity because never again in your life will you be surrounded by all smart people. This is very unusual and creates some interesting situations. In the real world, you will of course find smart people, but also some who are not, and this fundamentally separates the Caltech undergraduates from others.

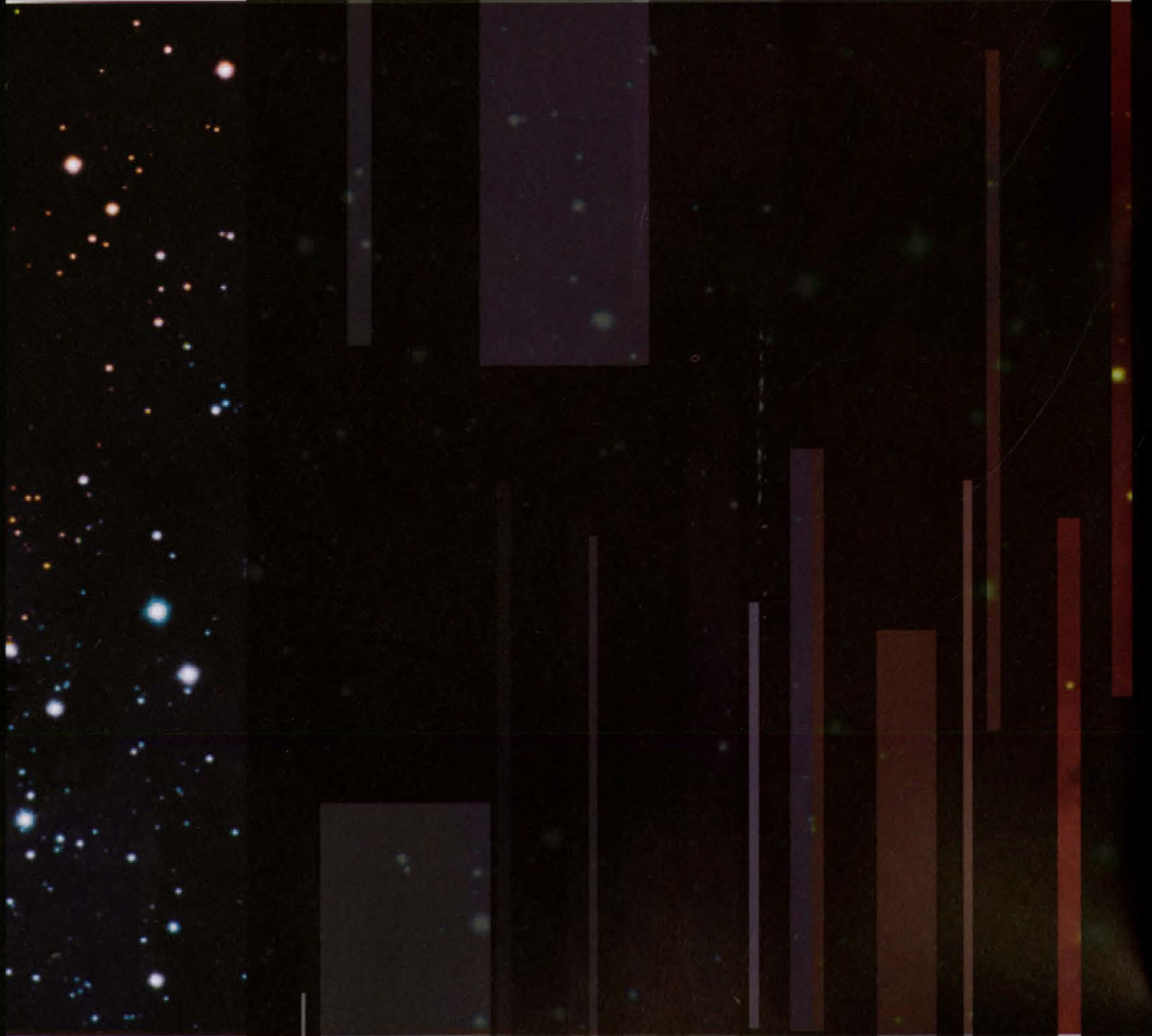
How do you feel the undergraduate and graduate experience at Caltech should differ, and how can the disconnection between the two be improved?

First of all, the two are not entirely disconnected. Undergrads get to know a number of grad students through both TAs and RAs. Furthermore, there are also many musical groups and other clubs that involve a mixing of undergrads and grad students.

I think the difference between the two experiences lies in the nature of the positions. Graduate students are highly focused on working with their advisor on one particular research issue. The undergrad experience is more getting a sampling of many different disciplines. There is also a difference because graduate students are basically beginning a career. They remain focused on learning and are still students first; however, they are starting to develop their skills as professionals.

CURJ's goal is to publish significant undergraduate research. What are some of your views on undergraduate research experiences, and how does it shape future scientists?

To me, getting involved in research as an undergrad is the best way to learn about what being a scientist is about. Even if you take the courses in your field, learn everything, and get good grades, it's still not the same as doing your own kind of research through a program such as SURF. At lectures, students.



Searching for Evidence of Planet Formation in p Ophiuchus — Applying a Period-Searching Algorithm to Near-Infrared Time-Series Photometry

Alan H. Gee¹

Peter Plavchan¹

Introduction

On any given night, there are countless stars in the night sky. With so many stars to be seen, where are all the planets? Currently, technology cannot distinguish between the faint light intensity of planets and their bright host stars. This makes direct imaging of planets difficult and increases the need for techniques using indirect evidence to detect planetary existence. These indirect techniques have been used to find more than 250 known extrasolar planets. When planets or other stellar masses interact with young stars, photometric or spectroscopic signatures can be detected, like the reactionary wobble of the host star.

Thus, we can infer the presence of stellar, substellar, or planetary companions through photometric variability. By analyzing the photometric variability of these stars, stellar companions, like planets, can be found.

Young stellar objects (YSOs) are typically <5 Myr stars. A defining characteristic of a YSO is the chaotic environment, which includes magnetic fields, dust shells, dust disks, and ionized winds, that may surround a star (Montmerle et al. 1993). In addition, YSOs are enclosed by a cloud of rotating gas and dust, or a circumstellar disk, and as the star ages, this disk dissipates. Currently, the physical mechanisms responsible for this dissipation are not yet quantified. One unproven hypothesis for disk dissipation is planet formation (Meyer et al. 1997). Smaller masses can aggregate into larger “oligarchs” or proto-planets with sufficient mass in dust and gas that can cool and condense into planets. YSOs are prime candidates for hosting proto-planets. However, there is no direct observational evidence that shows planet formation in progress.

To begin looking for planets, we first need to find stars with periodic photometric variability. We can associate periodic variability with the Keplerian orbital period of unseen companions. This is done by investigating changes in a star's emitted light intensity, indicating interaction between the star and its magnetic fields and/or circumstellar material. YSOs can exhibit photometric variability due to accretion, stellar rotation, eclipses, and veiling from disks and interstellar material. Differentiating the variability of YSOs through the near-infrared J, H, and Ks light bands can distinguish between these physical mechanisms. In search for these mechanisms, a novel period-searching algorithm has been devised. Using the algorithm, we executed a photometric variability search on ~1600 sources in ρ Ophiuchus using data from the 2MASS Calibration Database. Additionally, we devised a significance threshold to filter the results from the period-searching algorithm, distinguishing potential binary systems.

After analysis of light and color curves produced by our algorithm, up to 39 possible sources with significant periodic variability were identified. One source of particular interest, WL 4, has an ~65 day periodic light curve with the variability that can be directly attributed to an unseen companion interacting with the surrounding circumstellar disk. In addition, two other sources, YLW 16A and GY 241, have evidence for a proto-planetary system. The period-searching algorithm and its significance characterization have produced the discovery of YSOs with a stellar companion and possibly proto-planets; perhaps, additional searching may reveal more sources with forming planets.

Finding Stellar Companions

A first step to understanding planet formation involves finding stars with regular variability periods as objects passing in front of stars change the perceived light intensity. This method can lead to discoveries of stellar companions or even planets. Previously, in the case of DQ Tau (Mathieu et al. 1997), periodic variability revealed the presence of a stellar companion. Variability studies of more YSOs are needed to elucidate the processes involved in circumstellar disk evolution with or without the presence of stellar companions or nascent planetary systems.

One interesting star-field is ρ Ophiuchus (ρ Oph), a ~150 parsec star-forming region containing several hundred ~1 Myr old YSOs (Barsony et al. 2005; Natta et al. 2006; Lada 1987; Lada & Wilking 1984). Preliminary studies of ρ Oph have found photometrically variable sources (Plavchan et al. in press). In Plavchan et al. (in press), a pilot study was conducted on ~5% of the stars in the ρ Oph field using data collected by the Two Micron All-Sky Survey Calibration Point Source Working Database (2MASS Cal-PSWDB). In the initial study, two YSOs that demonstrate a regular variability period were identified using a novel period-searching algorithm (Plavchan et al. in press). Using the same

algorithm, the results presented in this study were generated by analyzing the full data set from the 2MASS Cal-PSWDB of ρ Oph, covering 0.13 square degrees. With this data, the significance of the period-searching algorithm can be empirically characterized, identifying more periodic sources in an easier manner.

“When planets or other stellar masses interact with young stars, photometric or spectroscopic signatures can be detected, like the reactionary wobble of the host star.”

Scanning the Skies

Choosing a Target

The Two Micron All-Sky Survey (Skrutskie et al. 2006, 2MASS) imaged the entire sky of ρ Oph in three near-infrared bands, J, H, and Ks, between 1997 and 2001. Hourly observations of 35 fields were used to perform a photometric calibration for 2MASS. Six consecutive scans of the calibration field were made in alternating declination directions in ~10 minutes of elapsed real time. These six observations compose a scan group, which is used instead of the individual scans to minimize short time variation. The 2MASS survey measured 1582 independent scans of the field, or 264 scan groups, in ρ Oph. The same automated processing system was used to extract photometry from the raw imaging data in the calibration observations as was used for the general all-sky survey (2MASS PSC). All the data scans were loaded into the 2MASS Cal-PSWDB (Cutri et al. 2006). Using individual observations collected from the aperture photometry of the 2MASS Cal-PSWDB, only sources with 50 or more detections were selected for closer study. Sources with <50 detections could not be used because these sources have poor photometric quality and are not bright enough for our data analysis techniques. Thus, the investigation begins with 1678 sources in ρ Oph, consisting of 395,750 individual photometric measurements over all epochs, sources, and bands (100,000-150,000 per band).

The Period-Searching Algorithm

From the field of ρ Oph, our goal is to find stars that exhibited periodic photometric variability, similar to characteristics of an orbiting companion star or a large planet. The premise is that, as an object orbits the star, various changes in light intensity and color can be observed. This photometric

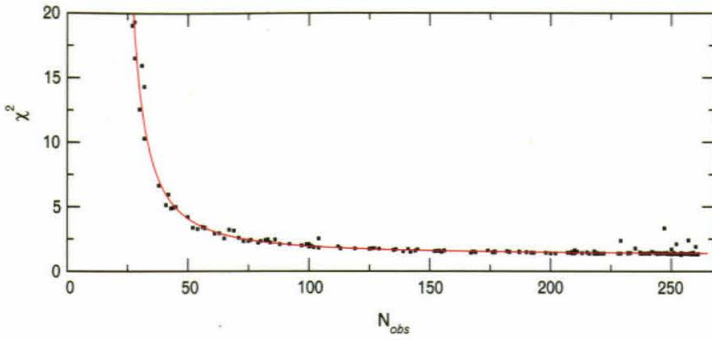


Figure 1. Graph of the $\chi_{n_0}^2$ value as a function of detection size, N_{obs} , for the test case with the parameters: $n_0 = 25$ and $p = 0.06$. This function,

$$f(N_{obs}) = \left(\frac{62.5495}{N_{obs} - 18.4963} \right)^{1.5} + 1.2523,$$

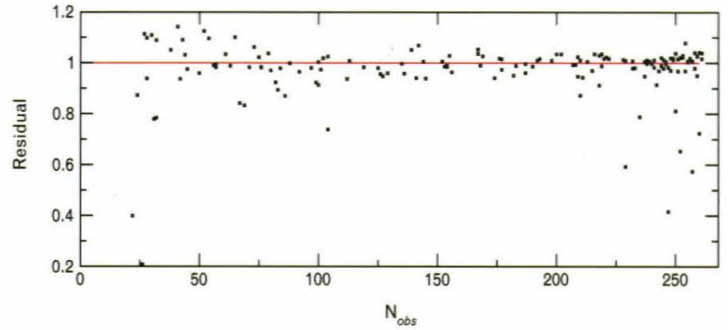
phenomenon can be revealed more easily with an innovative period-searching algorithm used to detect periodic variability in stellar objects (Plavchan et al. in press). The algorithm begins by investigating tens of thousands of possible periods between 0.1 and 100 days, with a uniform frequency sampling, for each source in the field. Then for each period, P_j , a folded light curve, which depicts the amount of light emitted by a source as a function of time, is generated from the time-series photometry. These light curves are used to determine the correct period or a fractional multiple of the period.

The algorithm uses a specified phase window, p , to look for the best smooth fitting curve, which helps remove short-period signals or flickering. A phase is defined as the time (t_i) modulo the period (P_j). We assume that any periodicity will be approximately continuous and smoothly varying over one period cycle. This process generates a smoothed light curve and is used as the prior, or reference, source to compare with our light curve. A $\chi_{n_0}^2$ value is computed for each source:

$$\chi_{n_0}^2 = \frac{\sum_{i=1}^{n_0} J_i - J_{mean}}{\sum_{t=1}^{n_0} (J_t - J_{prior_t})^2} \quad (1)$$

where J is the band magnitude data. The prior term (J_{prior_t}) is the mean of J_i if the phase, ph_i , of J_i for trial period P_j is within $\frac{1}{2}$ of the phase window, p , of the phase, ph_t , for J_{prior_t} . In other words, if $ph_t - \frac{1}{2}p \leq ph_i < ph_t + \frac{1}{2}p$, then J_i is included in the average smoothing that generates J_{prior_t} .

Equation (1) is the normalization function where the algorithm measures how the prior improves the fitted curve compared to a straight line and gives a $\chi_{n_0}^2$ for every period. We maximize the $\chi_{n_0}^2$ using the n_0 worst fit data points as we want to find the period in a "worst-case" scenario. So, the best periods we use for our fits are ones with the largest $\chi_{n_0}^2$ value. We



is the best-fit function where the residuals have been minimized. This is one example where the 1.5 power law models the behavior of the period-searching algorithm as a function of the parameters. Note the outlier sources with residuals < 0.8 were excluded from the fit because they are periodically variable.

empirically characterize the dependence of the period-searching algorithm on p and n_0 to quantify the significance of $\chi_{n_0}^2$.

Data Modeling

With the targets identified, the period searching algorithm was applied to each source. For computational efficiency, a random subset of ~ 180 sources with an evenly distributed range of data observations, N_{obs} , was selected for developing the significance threshold for the period-searching algorithm. The algorithm depends on three given parameters: n_0 , p and N_{obs} . Using a monte carlo simulation of 15 test cases consisting of varying n_0 and p , the $\chi_{n_0}^2$ significance value for the subset of our data was computed. Ultimately, the $\chi_{n_0}^2$ distribution as a function of N_{obs} was generated and determined to have the functional form:

$$F(N_{obs}) = \left(\frac{a}{N_{obs} - b} \right)^{1.5} + c \quad (2)$$

where a , b , and c represent real numbers (Figure 1). However, the power law with an index of 1.5 broke down for $n_0 < 12$ and/or $p < 0.04$ when dealing with a low number of detections as a smaller power law was more appropriate. Because there are other algorithms that specialize in finding periodic sources at low number of detections (~ 20 , Dworetzky 1983), the parameters for the algorithm was constrained to $12 < n_0 \leq 250$, and $0.04 < p \leq 0.5$.

To compose the best-fit functions, the functional fits for the parameters were tested empirically, rather than analytically, by minimizing the calculated residuals. The residuals, which were calculated as the predicted function value divided by the observed value, were minimized using a pseudo- χ^2 minimization. Next, all three values to Equation (2) were fit as a function of n_0 with p fixed and then as a function of p with n_0 fixed, generating six distinct plots. After characterizing the behavior of the six

plots and minimizing the residuals, we found these six best-fit functions:

$$f_a(n_0) = -0.3491(n_0 - 17.0796)e^{-0.0451n_0} + 63.4573 \quad (3a)$$

$$f_b(n_0) = 1.3023\left(1 - \frac{23.3762}{n_0}\right)e^{-0.0283n_0} + 18.4347 \quad (3b)$$

$$f_c(n_0) = 0.2796e^{-0.0381n_0} + 1.1467 \quad (3c)$$

$$f_a(p) = 82.6288e^{-12.1989p} + 25.4356 \quad (4a)$$

$$f_b(p) = 3.0791p^{-0.6377} \quad (4b)$$

$$f_c(p) = (p - 0.0305)^{-0.0395} + 0.0905 \quad (4c)$$

These six functions of one parameter were then combined into three functions of both parameters n_0 and p . Upon investigation, we assumed that the constant term of the n_0 function could be substituted by the entire p function. After preliminary testing of each combination, the constant term in the $f_c(p)$ function was dropped when combining it with $f_c(n_0)$. It is postulated that this particular constant term may relate to the n_0 component of the c parameter (see Equation (3c)). Thus after substitution, we have the following three functions to describe n_0 and p as a function of N_{obs} :

$$f_a(n_0, p) = -0.3491(n_0 - 17.0796)e^{-0.0451n_0} + 82.6288e^{-12.1989p} + 25.4356 \quad (5a)$$

$$f_b(n_0, p) = 1.3023\left(1 - \frac{23.3762}{n_0}\right)e^{-0.0283n_0} + 3.0791p^{-0.6377} \quad (5b)$$

$$f_c(n_0, p) = 0.2796e^{-0.0381n_0} + (p - 0.0305)^{-0.0395} \quad (5c)$$

where (5a), (5b), and (5c) are parameters of the following equation which follows from Equation (2):

$$F(N_{obs}, n_0, p) = \left(\frac{f_a(n_0, p)}{N_{obs} - f_b(n_0, p)}\right)^{1.5} + f_c(n_0, p) + 25.4356 \quad (6)$$

To test the validity of the function predictions, a second monte carlo simulation was conducted to empirically evaluate simultaneously varying n_0 and p with 18 test cases. The simulation showed that the predicted values are accurate with mean percent errors of $1.1\% \pm 3.4$ for f_a , $1.0\% \pm 3.5$ for f_b , and $0.1\% \pm 1.8$ for f_c (Table 1). These uncertainties are consistent with a good fit to the n_0 and p combined functions. Therefore, these equations are indeed adequate in predicting the parameters to describe any n_0 and p in the parameter space.

Significance

Using the empirical fits for a , b , and c on n_0 and p , it was determined that $n_0 = 40$ and $p = 0.06$ were ideal values for parameters. To compute the $\chi^2_{n_0}$ value (now χ^2_{40}), the K_s photometric band of the data was utilized for evaluating the 1679 sources with the algorithm. Using the above-mentioned parameters, the non-variable sources value of χ^2_{40} in the entire ρ Oph data set was fit with the function (Figure 2):

$$F(N_{obs}, 40, 0.06) = \left(\frac{63.8629}{N_{obs} - 18.6927}\right)^{1.5} + 1.2100 \quad (7)$$

It was determined that the sources below the functional fit were non-periodic ($\chi^2_{40} < F(N_{obs}, 40, 0.06)$), and these sources were then used to calculate the standard deviation, of the χ^2_{40} as a function of N_{obs} . In Figure 2b, it is apparent that the residuals for low number of detections have a larger spread than the residuals for high number of detections. As a result, the sources were grouped by every 25 N_{obs} when composing a standard deviation function to account for the larger spread in low number of detections. After fitting the function and minimizing the residuals, a function consistent with a good fit was obtained (Figure 3):

$$\sigma(N_{obs}) = \frac{2.3790}{N_{obs} - 21.6449} + 0.0105 \quad (8)$$

Next, σ was used to determine the threshold at which the periodic sources begin to appear. By inspection of the light curves, this threshold was established:

$$\frac{\chi_i}{F(N_{obs}, n_0, p)} - 1 > 6\sigma(N_{obs}) \quad (9)$$

Sources that satisfy this expression are considered periodic near-infrared variable sources and possible candidates for binary star systems or planetary association.

Table1. Monte Carlo Simulation: Testing Significance Funtion

n0	ρ	Obs. Param. A	Pred. Param. A	%Error ^a	Obs.Param. B	Pred.Param. B	%Error ^a	Obs.Param. C	Pred.Param. C	%Error ^a
12	0.25	31.338	30.382	-3.054	6.796	6.574	-3.259	1.205	1.239	2.815
13	0.04	80.893	76.952	-4.872	22.235	23.263	4.622	1.393	1.372	-1.500
15	0.06	64.109	65.547	2.243	17.776	18.042	1.500	1.308	1.307	-0.042
18	0.05	69.756	70.192	0.625	19.958	20.568	3.054	1.310	1.309	-0.054
18	0.06	63.138	65.036	3.006	18.173	18.284	0.610	1.287	1.290	0.208
25	0.06	62.550	64.284	2.772	18.496	18.560	0.343	1.253	1.257	0.337
25	0.4	25.656	25.169	-1.898	5.883	5.565	-4.602	1.135	1.148	1.136
25	0.1	49.530	48.938	-1.194	13.192	13.411	1.661	1.200	1.219	1.602
25	0.04	79.775	75.265	-5.653	22.927	24.024	4.784	1.290	1.310	1.534
40	0.06	62.172	63.863	2.719	18.604	18.693	0.479	1.208	1.210	0.194
60	0.24	29.562	28.859	-2.378	8.219	7.796	-5.145	1.128	1.092	-3.168
75	0.055	68.359	66.993	-1.998	18.500	19.682	6.390	1.157	1.174	1.423
125	0.3	28.994	27.429	-5.397	6.329	6.666	5.334	1.080	1.055	-2.269
140	0.45	24.910	25.700	3.171	5.127	5.144	0.335	1.067	1.036	-2.884
175	0.14	43.597	40.392	-7.351	10.569	10.796	2.143	1.090	1.092	0.145
180	0.05	71.813	70.318	-2.082	20.056	20.808	3.751	1.147	1.168	1.867
200	0.06	63.461	65.170	2.694	18.439	18.522	0.451	1.145	1.149	0.385
240	0.4	26.132	26.062	-0.268	5.800	5.525	-4.742	1.070	1.040	-2.794

^aNegative%errorsindicate that the significance function underestimates the actual value.

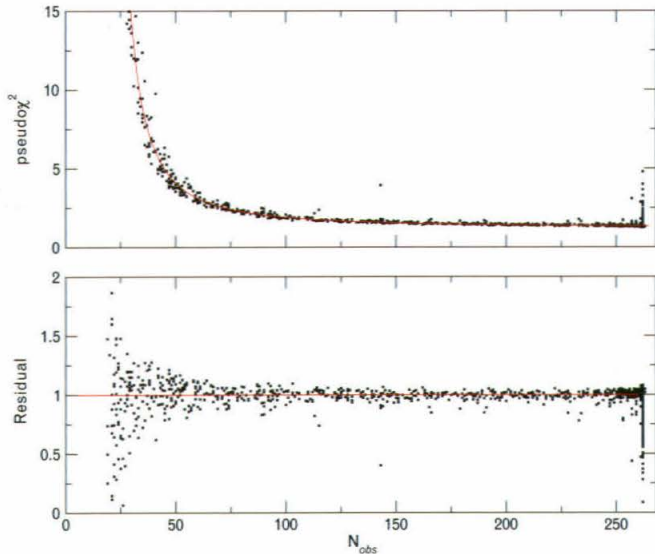


Figure 2. Graph of the $\chi^2_{n_0}$ value as a function of detection size, N_{obs} , with the parameters $n_0 = 40$ and $p = 0.06$ for the entire data set. The function (see Equation 7) is derived from the 3 combined functions (see Equation 5a, 5b, and 5c). For clarity, the top graph shows sources with low $\chi^2_{n_0}$ values. The lower graph displays the residuals (predicted function value/observed value). The red line represents the derived function in the top graph. notice the sources above the purple red are non-periodic and sources below the red line are possible periodic sources.

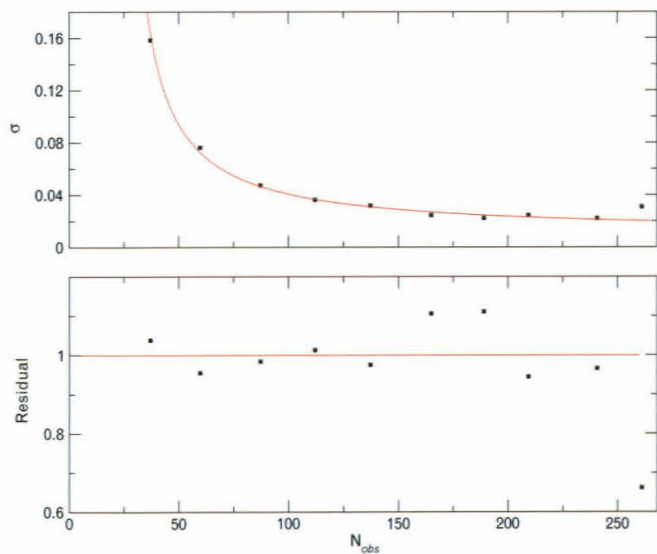


Figure 3. Graph of the standard deviation of the non-periodic sources as a function of the number of detections, N_{obs} . The function (see Equation 8) is derived from the non-periodic sources in the entire dataset (see sources above the red line in the residual plot of Figure 2). The lower graph displays the residuals (predicted function value/observed value). The red line represents the derived function in the top graph. Most of the periodic sources have $N_{obs} > 250$ because these sources in our sample are bright and are detected in all or nearly all scan groups.

Table 2. Periodic Sources Characterized by Significance Function

RA	De	N_{obs}^a	Period (days)	J^b (mag)	H^b (mag)	K_s^b (mag)	Significance (in terms of σ)
246.827026	-24.484921	262	65.5000	14.518 \pm 0.001	11.326 \pm 0.001	9.511 \pm 0.001	97
246.768814	-24.716524	262	3.5285	12 \pm 0.001	10.478 \pm 0.001	9.821 \pm 0.001	70
246.866684	-24.65926	257	92.7000	17.285 \pm 0.028	13.535 \pm 0.002	10.217 \pm 0.001	62
246.768997	-24.70384	262	14.5224	12.271 \pm 0.001	10.58 \pm 0.001	9.831 \pm 0.001	56
246.803055	-25.067175	262	0.8314	10.637 \pm 0.001	9.761 \pm 0.001	9.373 \pm 0.001	53
246.87851	-24.790745	262	1.2450	12.181 \pm 0.001	10.385 \pm 0.001	9.474 \pm 0.001	50
246.85556	-25.105873	262	0.4851	15.455 \pm 0.002	14.988 \pm 0.002	14.825 \pm 0.003	48
246.84552	-24.299223	262	5.5386	13.31 \pm 0.001	10.692 \pm 0.001	9.39 \pm 0.001	36
246.879456	-24.567505	262	3.5550	13.422 \pm 0.001	11.317 \pm 0.001	10.327 \pm 0.001	34
246.852737	-24.493141	262	6.5787	17.416 \pm 0.077	14.824 \pm 0.002	12.47 \pm 0.001	27
246.840942	-24.726538	262	6.3601	17.237 \pm 0.011	13.198 \pm 0.001	10.762 \pm 0.001	26
246.743301	-24.358301	262	6.0286	16.218 \pm 0.003	13.164 \pm 0.001	11.488 \pm 0.001	25
246.784149	-24.707903	262	4.9793	15.365 \pm 0.001	12.252 \pm 0.001	10.723 \pm 0.001	24
246.773605	-24.670246	262	0.6838	17.455 \pm 0.093	16.343 \pm 0.01	13.898 \pm 0.001	24
246.79657	-24.679569	262	0.9924	17.082 \pm 0.008	13.223 \pm 0.001	10.563 \pm 0.001	21
246.813034	-24.860764	262	0.8891	10.656 \pm 0.001	9.808 \pm 0.001	9.467 \pm 0.001	21
246.862778	-24.538191	262	1.0533	17.371 \pm 0.038	14.454 \pm 0.001	12.375 \pm 0.001	20
246.859558	-24.712914	262	3.7206	17.433 \pm 0.086	15.218 \pm 0.002	12.604 \pm 0.001	20
246.815674	-24.645327	253	0.9932	14.257 \pm 0.002	11.55 \pm 0.002	10.074 \pm 0.001	14
246.764984	-24.33481	262	3.9683	16.944 \pm 0.006	14.768 \pm 0.002	13.464 \pm 0.001	13
246.736557	-24.230934	253	0.8929	12.352 \pm 0.001	10.378 \pm 0.001	9.298 \pm 0.001	12
246.816208	-24.420513	262	2.9468	17.343 \pm 0.114	15.921 \pm 0.005	13.25 \pm 0.001	12
246.800537	-24.58028	262	0.7511	15.738 \pm 0.002	13.162 \pm 0.001	11.561 \pm 0.001	12
246.769058	-24.454285	262	5.9294	16.454 \pm 0.003	13.07 \pm 0.001	11.175 \pm 0.001	12
246.791824	-24.486958	262	4.1898	16.649 \pm 0.004	15.116 \pm 0.002	14.181 \pm 0.002	11
246.777481	-24.696856	262	0.7386	12.386 \pm 0.001	11.331 \pm 0.001	10.705 \pm 0.001	11
246.762512	-24.437368	262	0.9830	17.375 \pm 0.1	15.621 \pm 0.003	12.544 \pm 0.001	11
246.841599	-24.494326	262	0.4297	17.506 \pm 0.142	15.346 \pm 0.003	12.838 \pm 0.001	10
246.826492	-24.914923	262	0.7346	11.482 \pm 0.001	10.566 \pm 0.001	9.954 \pm 0.001	10
246.814423	-24.444342	262	3.9824	17.257 \pm 0.012	13.281 \pm 0.001	10.621 \pm 0.001	10
246.787857	-24.200172	262	3.4370	12.487 \pm 0.001	10.746 \pm 0.001	9.857 \pm 0.001	10
246.864105	-24.521235	262	11.7400	12.363 \pm 0.001	10.368 \pm 0.001	9.306 \pm 0.001	9
246.860397	-24.65638	262	1.1418	15.631 \pm 0.002	12.043 \pm 0.001	9.85 \pm 0.001	9
246.739288	-24.830378	259	1.0060	12.508 \pm 0.001	10.87 \pm 0.001	10.181 \pm 0.001	8
246.869705	-24.90884	262	0.8804	12.584 \pm 0.001	11.988 \pm 0.001	11.703 \pm 0.001	8
246.743011	-25.178873	257	1.2057	12.367 \pm 0.001	11.669 \pm 0.001	11.415 \pm 0.001	7
246.878784	-24.459188	257	1.0138	17.649 \pm 0.103	16.708 \pm 0.127	15.059 \pm 0.005	7
246.809784	-24.525482	262	0.9925	17.35 \pm 0.046	16.251 \pm 0.008	15.125 \pm 0.004	6
246.805267	-24.692636	262	0.4979	17.207 \pm 0.009	12.396 \pm 0.001	9.593 \pm 0.001	6

New Companions to YSOs

Evaluating the sources using the described algorithm above, the significance value of each source was analyzed along with their photometric magnitudes and their level of significance. This significance function in conjunction with a > 6 significance threshold determined that, at most, 39 sources possess significant periodic variability (Table 2). From this initial list of sources, three sources (Figures 4, 6, 7) have confirmed companions because of their long periodic variability and unique pho-

tometric changes which occurs from interactions with circumstellar disks and stellar companions. More specifically, two of the three sources, YLW 16A and GY 241, may have a proto-planet companion (Figure 6, 7). Forty-two sources were found to have significant periods but were filtered out because of the influence of seeing correlated variability (Plavchan et al. in press). Other sources were marked as false positives because of their periods corresponding to stellar rotation and data outliers.

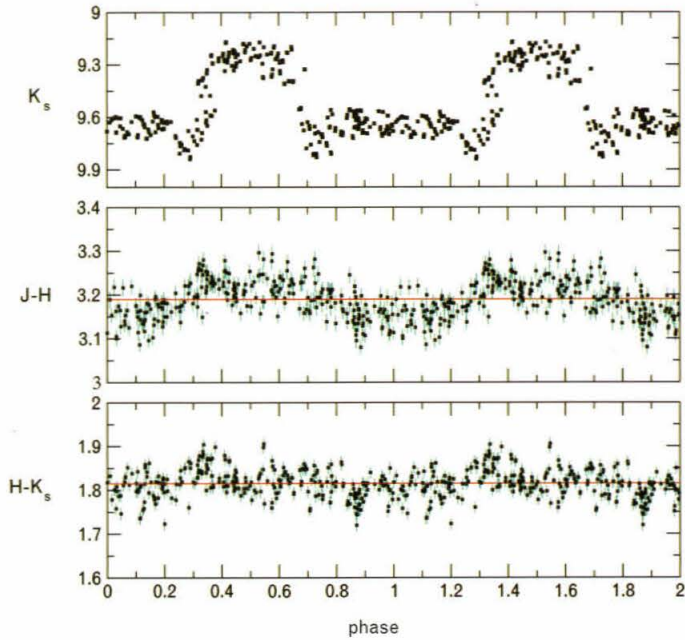


Figure 4 Light curve (K_s band) and color curves (J-H and H- K_s bands) of WL 4 folded to a period of 1565.50 days. In the K_s band, we see that the light variability is clearly periodic. We also see that when the source get brighter (positive slope in K_s graph), the source gets redder (red is toward the top of the graph, and blue is towards bottom of the graph) in both the J-H and H- K_s color bands. The blue lines indicate error bars.

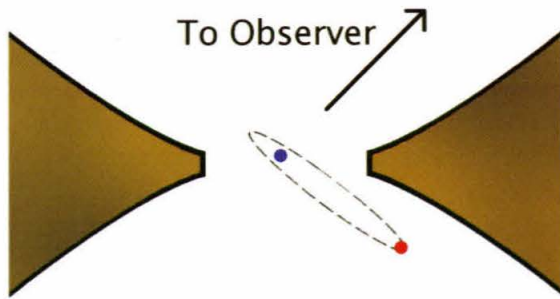


Figure 5. Schematic diagram of the model for WL 4. WL 4a (primary) is shown as a blue circle and WL 4b (secondary) as a red circle. A hypothetical orbit for WL 4b is shown as a dashed black line, approximately to scale. A flared circumbinary disk is shown in brown, inclined relative to the orbit of the binary. The arrow represents the direction from which we are observing WL 4 to explain the periodic veiling of WL 4b.

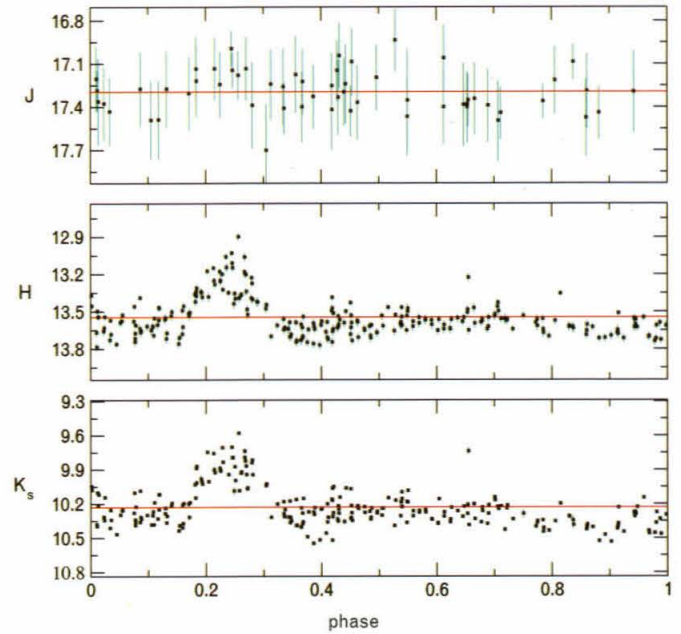


Figure 6 Light curve (J, H, K_s bands) for a periodic source, YLW 16A, located at right ascension 246.866684 and declination -24.65926. The period is calculated to be 92.7000 days with a significance of 62. This source shows the existence of a stellar companion, possibly a proto-planet, at phase 0.25.

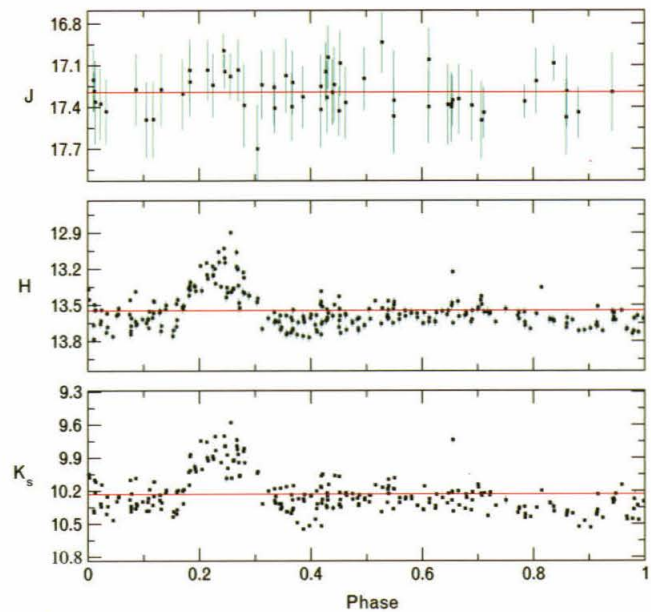


Figure 7. Light curve (J, H, K_s bands) for a periodic source, GY 241, located at right ascension 246.816208 and declination -24.420513. The period is calculated to be 2.9470 days with a significance of 12. This source shows the existence of an eclipsing binary system, possibly involving a proto-planet (phenomenon located at phase 0.35).



WL 4

WL4 possesses near-infrared photometric and color variability analogous to KH-15D, though the variability amplitude of 0.4 magnitudes for WL 4 is small relative to KH-15D. Additionally, it appears there is indeed a circumstellar disk surrounding our source WL 4. There is a peak-to-peak variation of 0.4 magnitudes in J, H and K_s, with a reddening of ~0.06 magnitudes in J-H and H-K_s when WL 4 is in the bright state. Also, the transition between bright and faint states, including the kinks in the light curve at phases of 0.28 and 0.72, last ~13 days. Such a long transition time can only be associated with a large spatial structure such as a circumstellar disk inner edge. Though WL 4 may not have a planetary companion, our period searching algorithm enabled us to narrow down one of many sources that are in a binary system. Further investigation of our other two sources, YLW 16A and GY 241, is needed to elucidate the nature of their potential proto-planetary companion.

Future Implications

Although the algorithm was successful so far, some improvements can be made. Filters can be incorporated to separate sources that are influenced by seeing-correlated variability, stellar rotation, or one point outliers. Currently, the function only distinguishes a source as significant based on its $\chi^2_{\tau_0}$ value without taking into account other factors that may falsely make a source periodically variable. This filter will help eliminate false positives and emphasize interesting sources.

Additionally, using the 2MASS Cal-PSWDB data in ρ Oph, we can generate a proper motion catalog of YSOs in the field. Proper motions will yield information about star formation region, dynamical evolution, and stellar origins. We also plan to conduct more in-depth near-infrared observations of the long-period periodic sources to obtain radial velocities, possible disk structure, stellar variability, and component masses. We will continue to characterize both periodic and non-periodic sources. Examining more candidate stars will inevitably lead to more exciting discoveries. Perhaps these discoveries might lead to the next Earth.

References

- Badalian, H., & Erastova, L., 1970, *Astronomicheskij Tsirkulyar*, 591, 4
- Barsony, M., Ressler, M., & Marsh, K., 2005, *ApJ*, 630, 381
- Chiang, E. I., & Murray-Clay, R. A. 2004, *ApJ*, 607, 913
- Cutri, R., et al., 2006. Explanatory Supplement to the 2MASS All Sky Data Release and Extended Mission Products.
<http://www.ipac.caltech.edu/2mass/releases/allsky/doc/explsup.html>
- Dworetsky, M., 1983, *MNRAS*, 203, 917
- Kusakabe, N., Tamura, M., Nakajima, Y., Kandori, R., Ishihara, A., Nagata, T., Nagayama, T., Nishiyama, S., Baba, D., Sato, S., Sugitani, K., Turner, E. L., Abe, L., Kimura, H., Yamamoto, T. *ApJ*, 632: L139-L142, 2005.
- Lada, C. J. 1987, in *IAU Symp. 115, Star Forming Regions*, ed. M. Peimbert & J. Jugaku (Dordrecht: Reidel), 1
- Lada, C. J., & Wilking, B. A. 1984, *ApJ*, 287, 610
- Mathieu, Robert D.; Stassun, Keivan; Basri, Gibor; Jensen, Eric L. N.; Johns-Krull, Christopher M.; Valenti, J. A.; Hartmann, L. W. *Astron J.* 113(5): 1841-1854, 1997.
- Mathioudakis, M. & Doyle, J., 1993, *A&A*, 280, 181
- Meyer et al., 1997, *AJ*, 114, 288.
- Montmerle, T., Feigelson, E., Bouvier, J., & Andre, P. 1993, in *Protostars and Planets III*, ed. E. H. Levy & J. L. Lunine. Univ. Arizona Press, 689
- Natta, A., Testi, L., & Randich, S., 2006, *A&A*, 452, 245
- Plavchan, P., Jura, M., Kirkpatrick, D., Cutri, R., Gallagher, S.C. 2008, *ApJS*, [In press].
- Plavchan, P., Gee, AH., Stapelfeldt, K., & Becker, A. *ApL*, 2008 [Submitted].
- Rebull, L. 2001, *AJ*, 121, 1676.
- Skrutskie, M., et al., 2006, *AJ*, 131, 1163
- Watson, A. and Stapelfeldt, K., 2008, *AJ*, 133, 845
- Winn, J.N., et al., 2006, *ApJ*, 644, 510
- Winn, J.N., Holman, M.J., Johnson, J.A., Stanek, K.Z., & Garnavich, P.M., 2004, *ApJ*, 603, L45



Making Sure Advanced LIGO Will Be Clean Enough to Hear the Big Bang

Edward Macaulay

Radical Implications of an Unexpected Prediction

Albert Einstein's theory of General Relativity has proven spectacularly successful in its agreement with the most precise measurements of astrophysical phenomena. A curious prediction of the theory, which Einstein noticed in 1918, was that almost any accelerating mass would radiate waves – gravitational waves – which travel at the speed of light, and cause vibrations in the position of everything through which they pass.

For nearly 70 years, gravitational waves were a hotly contested prediction – even Einstein managed to briefly convince himself that they didn't exist. Tantalisingly, gravitational waves would have radical implications should they be discovered: since the frequency and amplitude of the vibrations caused by gravitational waves are directly related to the acceleration of the source, gravitational waves can be considered essentially a form of sound wave. Indeed, in principle, a strong enough gravitational wave could even be heard by humans. However, the typical volume of some of the loudest gravitational wave sources – such as a supernova, or the coalescence of a pair of neutron stars – is expected to be a staggeringly quiet minus two hundred and twenty decibels by the time the waves have reached the earth.

Nevertheless, the effects of gravitational waves could, in principle, be detected with an extremely sensitive microphone. The radical implications of such a discovery would be the ability to hear astronomical events such as supernovae, black hole inspirals, and even echoes from the Big Bang. However, for 70 years after Einstein first made his prediction, there was no empirical evidence to suggest that gravitational waves were anything more than a theoretical artifact of General Relativity. That is, until Russel Hulse and Joseph Taylor – astrophysicists at Princeton – indirectly proved the existence of gravitational waves by studying the orbit of a binary star system. They found that the system was losing its gravitational potential energy at exactly the rate that would be expected were the stars radiating gravitational waves. Meanwhile, Rai Weiss, of MIT, and Kip Thorne & Ron Drever, of Caltech, had worked out how to build, essentially, an extraordinary microphone that would be sensitive enough to directly detect the vibrations caused by gravitational waves: LIGO, the Laser Interferometer Gravitational Wave Observatory.

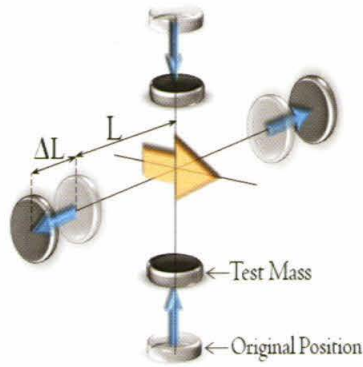


Figure 1: The gravitational wave effect

A gravitational wave travelling in the direction of the orange arrow causes test masses to oscillate between being squashed together and pulled apart on alternate axes. The amount by which the masses oscillate, ΔL , depends on how far the masses are separated by, L . The ratio of ΔL to L is known as the 'strain'.

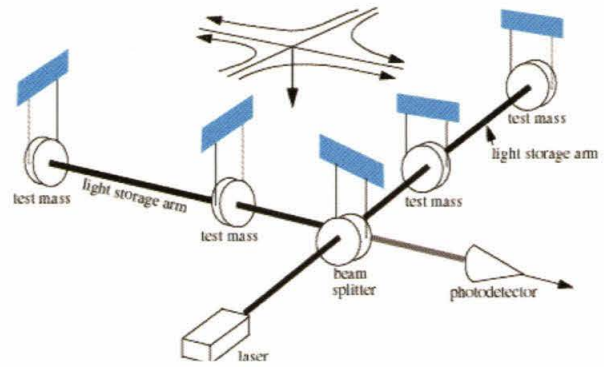


Figure 2: A Michelson interferometer, as used to detect gravitational waves. Taken from the online LIGO fact sheet.

Thinking of Everything

Fundamentally, what LIGO does is measure the vibrations of test masses, but its design takes advantage of the unique kinds of vibrations caused by gravitational waves, as shown in Figure 1.

LIGO plans to detect gravitational waves by using highly reflective test masses as the mirrors in an optical configuration known as a Michelson Interferometer, as shown in Figure 2

Laser light is split at a beam splitter and sent down the two perpendicular arms of the interferometer to the test masses. The length of one arm is set shorter than the other arm by exactly a quarter of the wavelength of the laser light, so that when the light is recombined at the beam splitter, the two beams cancel out exactly, and nothing is observed at the light detector. The idea is that when a strong enough gravitational wave comes by, the oscillations of the mirrored test masses stop the light from each arm canceling out exactly, and a signal is observed at the detector. LIGO has two detectors, one each in Livingston, Louisiana, and Hanford, Washington, to rule out false signals terrestrial vibrations.

The real difficulty in detecting gravitational waves is that the typical strain on earth extremely small. Einstein calculated that the gravitational waves due to some of the most violent events in the universe, such as the inspiral of two black holes, would only have a characteristic strain of about 10^{-21} . That is, for two test masses separated by one meter, the masses would only oscillate by a maximum of 10^{-21} m from their original position. To maximize the signal, the test masses in LIGO are separated by four kilometres, all of which is enclosed in beam tunnels kept at ultra high vacuum. Even so, the test masses are only expected to vibrate with a maximum displacement less than one thousandth the diameter of a proton! The list of in-

novations developed to actually measure these displacements is enormous. As my supervisor, Bob Taylor said, "When you're measuring down to 10^{-21} , you have to think of everything."

Just keeping the test masses isolated from terrestrial vibrations is a huge task. At the Livingston observatory, the vacuum enclosure is stabilized from microscopic seismic vibrations with active hydraulic feedback. Inside the vacuum, the test masses are suspended from passive isolation springs, which exponentially reduce the magnitude of any remaining vibrations. Finally, the test masses are hung by a wire loop to allow them to oscillate in response to gravitational waves.

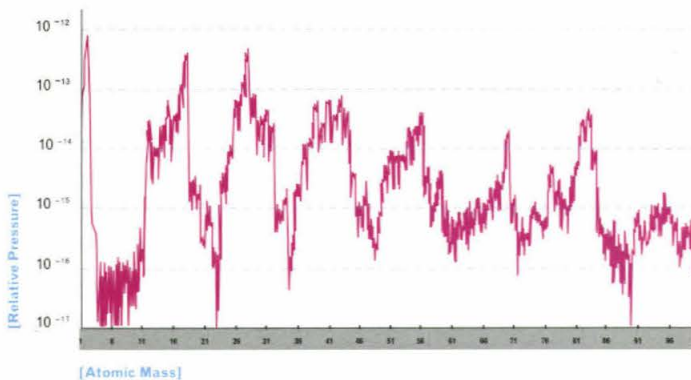
Even so, the displacement of the mirrors is twelve orders of magnitude smaller than the wavelength of light used in the interferometer, so LIGO has to use an extremely powerful laser in order to infer the displacement over the average of enough photons. But the heat of the laser causes the test mass mirrors to expand, so they're engineered with an extremely slight spherical concavity so that the mirrored surface becomes perfectly flat when the laser is at maximum power. And the entire interferometer is kept at the ultra high vacuum (UHV) of less than one billionth atmospheric pressure to keep the test masses still and minimize laser scattering in the arms.

But the UHV creates its own problems: it sucks dissolved gas or surface contaminants out of anything placed inside it. The process is known as outgassing, and it's exactly the same phenomenon as a vacuum cleaner lifting dirt off a surface, except on a much grander scale. Outgassing is very bad news for LIGO, as it leads to a residual atmosphere of contaminants in the UHV. The amount of light scattered or absorbed by residual contaminants in either arm is random, but if more light is absorbed in one arm than another, the net result is that the two beams don't exactly cancel out at the light detector. In prac-

tice, this scattering is forms a part of LIGO's 'noise budget' – it's strain sensitivity due to instrumentation limits. Even worse, if any contaminants make their way onto LIGO's test masses, the extra heat they absorb can cause the mirrors to warp out of their perfectly flat profile at maximum laser power – the only solution is to replace the offending test mass.

To keep LIGO's vacuum pure, everything which is placed inside the UHV, such as the seismic isolation systems, has to be rigorously qualified for outgassing. UHV materials have to be carefully chosen to start with – for example, regular steel is saturated with hydrogen, which seeps out under low pressure, so LIGO's beam tubes were made from special low outgassing steel. Next, any components destined for the UHV has to be thoroughly cleaned with solvents, to remove most of the surface contaminants (such as machining oil). Finally, the components are sealed into a separate vacuum chamber and exposed to ultra high vacuum. This allows any remaining contaminants to outgas safely without contaminating LIGO's ultra clean vacuum. The components can be heated to temperatures as high as 300°C while they're in the vacuum to ensure any contaminants evaporate off the surface – this process is known as vacuum baking.

A bonus of vacuum baking is that it provides a direct way to measure the contaminants that a component is outgassing. The residual atmosphere in the vacuum oven can be studied with a mass spectrometer, which provides a very good indication of the kinds of contaminants being outgassed.



The mass spectrometer displays the relative pressure of the residual atmosphere as a function of the atomic mass of the molecules that it consists of. [data taken from <http://www.ligo.caltech.edu/~rtaylor/> - should be able to find higher quality example of scan though]

A Vacuum Bake Oven:
the mass spectrometer is visible in the background
(the SRS RGA 200)



What's Really Needed

In spite of all the innovations in LIGO, observations indicate that a gravitational wave strong enough to be detected should only come along, on average, about once every thirty years. As such, Initial LIGO was always planned as a stepping stone to Advanced LIGO; an upgrade to Initial LIGO that should be able to detect gravitational waves from a thousand times more sources than before, and serve as a genuine gravitational wave observatory.

AdLIGO will occupy the same beam tubes as Initial LIGO, but almost all the internal components will be upgraded to provide greater sensitivity. AdLIGO has a lower operating pressure target – less scattering in the arms will reduce noise and increase sensitivity. Another part of the upgrade is improved seismic isolation – this makes it easier to identify vibrations due to gravitational waves, as opposed to terrestrial sources.

The problem is, a key component of the new seismic isolation system, the quadruple pendulum support, is actually too large to fit inside our vacuum bake ovens. This is actually a serious issue – the quad support is an essential component of the seismic isolation systems, but it must be qualified for outgassing to ensure it'll be within AdLIGO's pressure budget.

Initial LIGO also had some components that were too large to be vacuum baked – these were prepared in ultra clean air-bake ovens. To qualify these components for outgassing, the residual surface contaminants were extracted with solvents, and then analyzed with infrared spectroscopy by an outsourced lab. Once the lab returned the contamination report, the outgassing of the component was estimated with a cross correlation of the component's surface contamination and established outgassing rates for particular volumes of given contaminants.

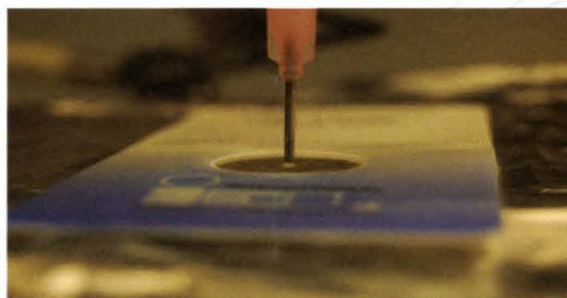
Performing the IR analysis at an outsourced lab isn't ideal – it's time consuming, and, in practice, it's invariably problematic to maintain a consistent calibration with outgassing rates determined in the bake lab. Furthermore, while AdLIGO strives for ever lower operating pressures, there's also an increasing need to add instrumentation to the UHV that can't be easily vacuum baked, such as electronic equipment. What's really needed is an 'in house' IR analysis method, which is what I was working on to develop last summer.

Developing a New Technique to Obtain Quantitative Results with FT-IR

I was using a Fourier Transform-Infrared Spectrometer (FT-IR) to find the infrared transmission spectrum of the contaminants. The FT-IR uses a Michelson interferometer (like the giant LIGO detectors, on a much smaller scale) to progressively select individual wavelengths of light from the broad spectrum of a tungsten filament. By collecting a spectrum with and without a sample in place (known as the background and sample spectra, respectively), the percentage of light transmitted at each

wavelength by the sample – its transmission spectrum – can be determined from the ratio of the two spectra. A convenient definition is the absorbance spectrum – the logarithm of the transmission spectrum – as this allows different spectra to be added and subtracted, instead of multiplied and divided.

For studying liquids, such as the solvent-contaminant solution, the solution has to be transferred with a pipette onto an IR transparent material in order to be placed in the spectrometer, for which we used disposable NaCl crystals. The background spectrum is then taken with a blank window in place, so that the transmission spectrum of the window is divided out of the sample spectra, leaving only the transmission spectrum of the sample.



Applying solution onto a spectrometer window with a pipette

Each individual contaminant has a unique absorbance spectrum; if a solution consists of a mixture of several different contaminants, then its absorbance spectra consists of a superposition of the constituent contaminants, scaled according to their proportion in the solution. If the spectra of the individual contaminants have been separately recorded, the composite spectrum can be numerically analyzed to determine the ratio of individual contaminants in the original solution.

Thus, FT-IR can determine what contaminants are present on a component, and their relative abundance. However, in order to estimate the total outgassing of a component, it's vital to know the total volume of each contaminant on the surface. To determine this, the fraction of light transmitted (or, equally, particular absorbance values) has to be calibrated to the associated volume of contaminant.

An essential constraint is that the method used to prepare the solution has to produce reproducible absorbance values when the solution is scanned. The conventional method is to sandwich the liquid solution between two spectrometer windows, separated by a gasket. As the depth of the solution is fixed by the gasket, the absorbance of the solution at a particular absorbance peak of the contaminant is directly proportional to the contaminant's concentration in the solution. The problem with using a fixed path length cell is that it

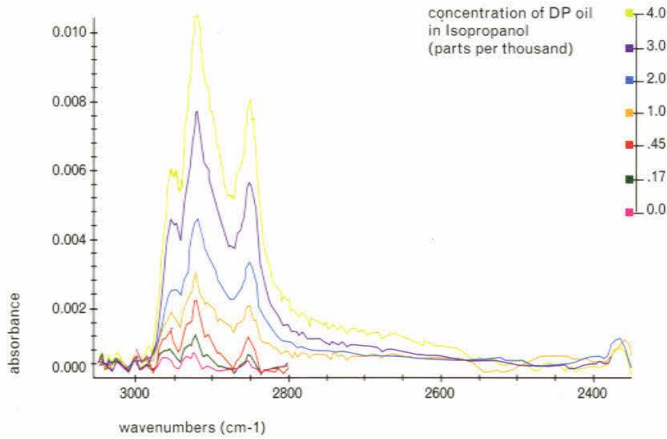


Figure 3: The Spectra of Different Concentrations of Dp Oil.

The functional form of each spectrum is the same, but the absolute absorbance scale is proportional to the concentration. The spectra were recorded with an empty sample compartment as the background – they should be compared to the spectrum of the blank slide (0.0 parts per thousand concentration). In principle, the blank slide should be completely clean of DP oil. However, the strong resemblance of this spectrum to the spectra with known concentrations of DP oil suggests that the blank slide has been contaminated with DP oil. Although this implies a systematic offset of the other spectra, it doesn't necessarily compromise the principle of using this method for quantification.

doesn't allow the solvent in the solution to evaporate off, so for low concentrations of contaminants, the final spectrum is dominated by the spectrum of the solvent – making it harder to discern the spectra of the contaminants. A fixed path length cell is fine if the solution being studied contains significant quantities of material other than solvent.

However, LIGO's components should be completely clean before going in the UHV, so ideally the sampling solution shouldn't contain any contaminants. To actually approve components for the UHV based on an FT-IR scan, it's important to be able to be sensitive to even trace quantities of contaminants, and essential to know the limit to which contaminants can be detected by FT-IR. Disposable FT-IR windows actually provide greater sensitivity to trace contaminants, as they allow the solvent to evaporate off. Also, as they're single use, they aren't contaminated from previous samples. The problem is, as the beam profile of the spectrometer is non uniform, an evaporated drop of solution will actually absorb different fractions of light depending on how the drop is distributed on the window. However, I found that applying a drop of solution with a pipette, by hand, to the centre of a spectrometer window is actually sufficient to obtain quantitative data.

I made up solutions of turbo pump oil (a common contami-

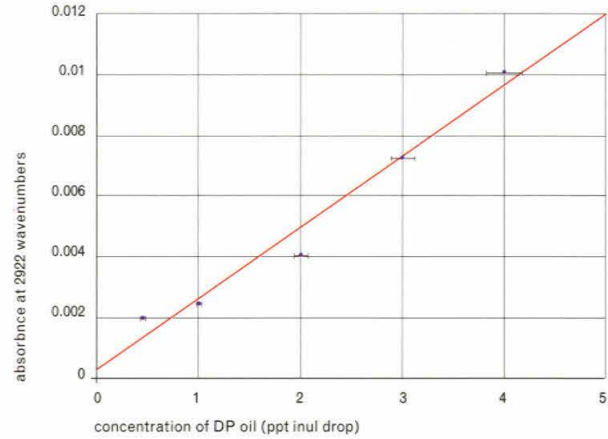


Figure 4: Linear Fit of Peak Absorbance.

This is a plot of the peak absorbance (at 2922 wavenumbers) of the spectra in Figure 1 as a function of their concentration, with a best fit line plotted in red.

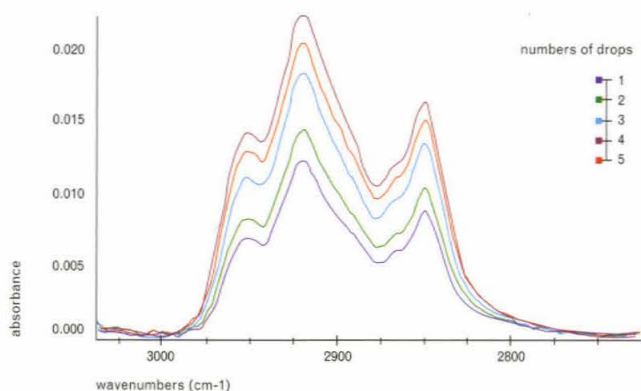
nant) in isopropanol, concentrated in the range 0.17 parts per thousand (ppt) to 4 ppt. A 2 micro litre drop of each solution was applied to the centre of separate spectrometer windows. The spectra are shown in Figure 3. As can be seen in Figure 4, the peak absorbance depends linearly on the original concentration of oil in the solution. As can be seen in Figure 3, the absorbance of the 0.17 ppt solution actually approaches the absorbance due to noise fluctuations in the spectrometer. There's some discretion as to precisely where the smallest detectable peak would disappear into the noise floor, but it appears to correspond to the absorbance of a 0.1 ppt sample. 0.1 parts per thousand of oil in a 2 micro litre drop corresponds to a total volume of 0.2 nanoliters – this is the smallest quantity of oil that must be collected onto the FT-IR window in order to make a detection.

This detection limit actually constrains how clean a component can be certified with FT-IR. Assuming that the method of sampling a component can collect a fraction x of the oil on a surface, then a surface area y of the component must be sampled in order to certify that the component contains less than $0.2(xy)^{-1}$ nLm⁻² of oil. We don't have any data yet on sampling efficiency, but it's likely to depend on the contaminant, the solvent, and the method used.

The Mystery of the Reducing Absorbance

To probe the detection limit of the spectrometer, the windows were only prepared with a single drop of solution. In practice, components could be sampled with several litres of solvent, which is then concentrated by evaporation. What remains would be a few mL of concentrated solution, which would have to be transferred to the spectrometer drop by drop with a pipette. The solution has to be applied slowly, so that the solvent can evaporate off between drops. As the drops are applied, a layer of contaminants slowly builds up on the surface – if the window is scanned between drops, the absorbance peaks slowly rise out of the noise floor as successive drops are added. It was while preparing a slide this way that I noticed that the peak absorbance sometimes decreased after additional drops were added.

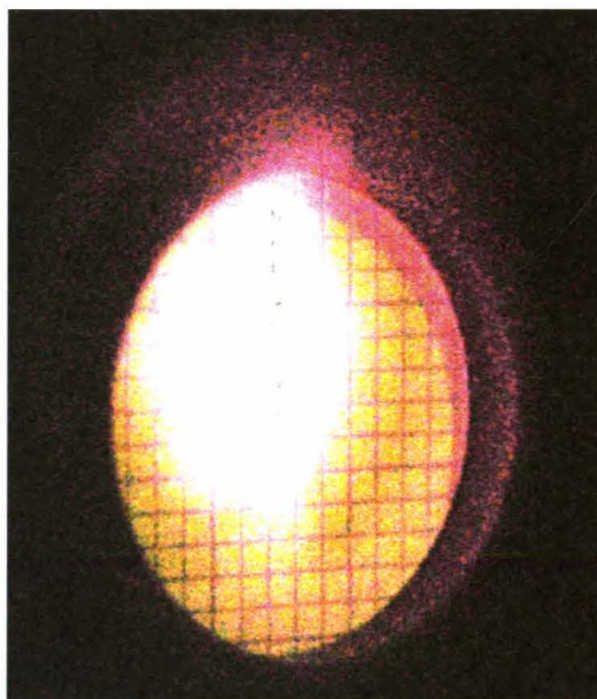
To verify this effect, I saved the spectra as 2 micro litre drops of a 5ppt solution of oil in isopropanol were successively added to a window.



The spectra of turbo pump oil, scanned as successive drops are added.

The absorbance increases, as expected, for the first four drops, but, unexpectedly, the absorbance decreases significantly after the 5th drop is added. We suspect this may be due to a non uniform beam profile in the spectrometer. To verify this, graph paper was placed in the spectrometer's window holder, and photographed with an IR sensitive camera.

While the entire aperture is diffusely illuminated, the beam is concentrated in a roughly circular region 11mm in diameter. We suspect that the oil molecules may have been originally contained within the brightly illuminated region, and then washed into the diffusely illuminated region by successive drops, where any contaminant molecules would absorb exponentially less light. As such, a new window holder should be engineered, with only an 11mm aperture. By applying smaller drops, and ensuring the drops remain within the 11mm aperture, we should be able to ensure that reproducible absorbance values are obtained.



The spectrometer's window aperture – graph paper has been added in place of a window. The length of each square is 1.27 mm (1/20th of an inch).

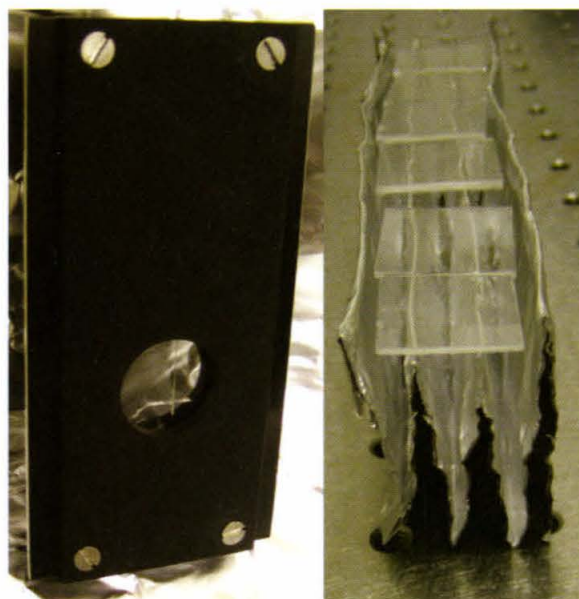
Outgassing Calibration

As demonstrated here for turbopump oil, we should be able to use FT-IR to obtain quantitative estimates of trace contamination on components. The method needs to be expanded for other substances, by individually collecting spectra over a range of volumes for all the other contaminants of concern to LIGO. The method may need to be refined further for 9mm diameter windows. However, the real quantity of concern to LIGO is the outgassing rate of a component.

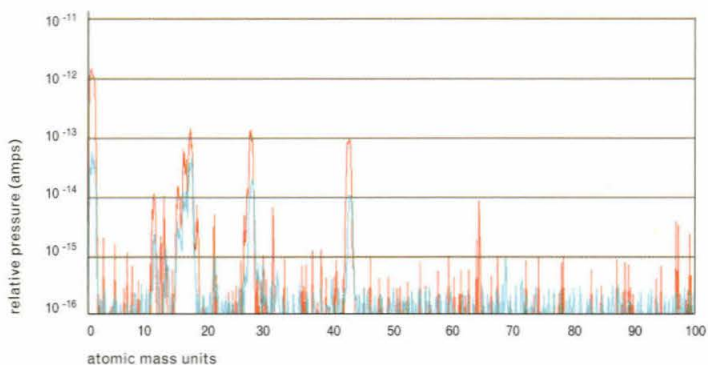
While FT-IR can identify molecules, it can't provide any data on how they'll outgas in UHV. The only way to determine outgassing rates is to vacuum bake a test component, contaminated with a controlled volume of material, and observe the associated outgassing rate with a mass spectrometer. By repeating this process over a range of contaminant volumes, peak absorbance on an FT-IR spectrum can be calibrated to particular outgassing atomic mass units (AMUs).

We decided to use the NaCl spectrometer windows as our 'test components', as this will eventually allow us to scan exactly the same contaminants with the FT-IR and mass spectrometer. As the NaCl windows come in cardboard holders (so they can be easily mounted in the spectrometer), the crystals were first removed from the cardboard, so they could be vacuum baked. Custom anodized stainless steel holders were made so the crystals can be scanned in the FT-IR.

Six windows were extracted, and cleaned with spectrometer grade methanol before being vacuum baked at 50 degrees Celsius for 48 hours. They were placed on a UHV foil tray for support. The outgassing was then recorded with mass spectrometer scan. A 2 micro litre drop of a 1ppt solution of DP oil in isopropanol was placed on two of the windows. One of the windows was then placed in the custom window holder, and scanned with the FT-IR.



The custom slide holder (left) and the NaCl crystals ready to be baked



The foil tray of windows was then returned to the vacuum bake oven. The window which had been FT-IR scanned was not returned to the oven, in case it had picked up additional contaminants from the slide holder. The remaining five windows were vacuum baked, as before, then RGA scanned.

The RGA scans of the clean window and the contaminated window are shown in figure five – the clean window scan is plotted in red, and the contaminated window is plotted in blue. As can be seen, the clean windows appear to out-gas slightly more contaminants than the windows with the addition of DP oil. This is probably because the windows were not particularly clean to start with (they were attached to the cardboard with glue). Also, DP oil, which is a low outgassing material, may form a film that prevents outgassing of other materials present on the slide. In future, the windows should be solvent cleaned to remove glue residue, then vacuum baked first just for cleaning purposes, then vacuum baked again to obtain a control AMU spectrum. The amount of contaminants placed on the window should be increased until associated outgassing AMUs are clearly identifiable. Much work is still required for the outgassing calibration, but a new, 21/2 inch diameter vacuum bake oven is currently being assembled, which will be ideal for further calibration work.

Conclusions and Prospects

There's lots of work still required before FT-IR can be used to qualify parts for the UHV. Every contaminant needs to be scanned in the FT-IR, and then vacuum baked to find the associated outgassing AMUs. Also, the efficiency with which contaminants can be extracted from the surfaces of components needs to be thoroughly investigated. Eventually, the final method needs to be verified on small components which can also be vacuum baked. Nevertheless, FT-IR should be able to qualify parts for LIGO's UHV when no other method can be used.

Acknowledgements

I'd like to thank my supervisor Bob Taylor, and Riccardo DeSalvo for all their assistance.

Further Reading

Introduction to gravitational waves and LIGO:

"Catching Gravitational Waves." Cardiff University. <<http://carina.astro.cf.ac.uk/groups/relativity/research/index.html>>.

"LIGO Fact Sheet." Laser Interferometer Gravitational Wave Observatory. California Institute of Technology & Massachusetts Institute of Technology. <http://www.ligo.caltech.edu/LIGO_web/about/factsheet.html>.

LIGO Vacuum Requirements:

Albert Lazzarini, Fred Raab, David Shoemaker, Rainer Weiss, John Worden, Gary Sanders, Ligo Vacuum Compatibility, Cleaning Methods and Qualification Procedures, 3/13/03, LIGO-E960022-B-E

Coyne, Dennis. "Ultra-High Vacuum (UHV) for the Advanced LIGO Detector." Caltech. 30 Aug. 2007 <<http://www.ligo.caltech.edu/~coyne/AL/SYS/UHV.htm>>.

Dennis Coyne, Vacuum Hydrocarbon Outgassing Requirements, 9/1/04, LIGO-T040001-00

FT-IR Spectroscopy:

MICHELSON INTERFEROMETER & FOURIER TRANSFORM SPECTROMETRY. 8 June 2007. University of Washington. <<http://courses.washington.edu/phys331/michelson.pdf>>.

TQ Analyst User's Guide. Thermo Electron Corporation, 1992. 40-47.

Make a difference... Change the world?

Sandia National Laboratories is for people with a hunger and desire to make a difference, a passion to change the world. We're one of the top science and engineering laboratories for national security and technology innovation. Be a part of the team helping America secure a peaceful and free world through technology.

We have exciting opportunities for college graduates at the Bachelor's, Master's, and Ph.D. levels in:

- Nuclear Engineering
- Mechanical Engineering
- Electrical Engineering
- Computing Engineering
- Information Technologies
- Computer Science
- Chemistry
- Business Administration ... and more

We offer internship, co-op, and post-doctoral programs.



Sandia is an equal opportunity employer. We maintain a drug-free workplace.

NOBODY GETS CLOSER TO THE PEOPLE. TO THE DATA. TO THE PROBLEM.

At CNA we analyze and solve problems by getting as close as possible to the people, the data and the problems themselves in order to find the answers of greatest clarity and credibility – all to help government leaders choose the best course of action.

We have a professional, diverse staff of over 600 people working in a variety of critical policy areas – such as national security, homeland security, healthcare and education – and offer career opportunities for people with degrees in engineering, mathematics, economics, physics, chemistry, international relations, national security, history, and many other scientific and professional fields of study.

Diverse views, objectivity, imaginative techniques, process driven, results oriented, committed to the common good. Join us.

Ed McGrady, Research Analyst, Ph.D., Chemical Engineering

Anita Hattiangadi, Research Analyst, M.A., Economics

Bradford Ng, Research Analyst, Ph.D., Chemistry

Krystal Williams, Research Analyst, M.S., Applied Mathematics

Kathleen Ward, Research Analyst, Ph.D., Physiology and Biophysics



www.cna.org

High-Order Surface Modeling: Automatic Design of Projection Surfaces

Author: Brandt A Belson
Mentor: Professor Oscar Bruno
Post Doc: Randy Paffenroth

Introduction

Recorded history tells of how man once looked at the wings of birds with envy and dreamed of flight. From hang gliders in the 9th century to hot air balloons in the 18th century to sustained flight in the 20th century, today we have mastered a sophisticated command of the skies. Aviation has become an integral part of our daily lives through which produce is shipped, packages are delivered, and forest fires are extinguished.

The financial cost of these services and the payload of these aircraft vary greatly. The Boeing 737, priced at \$80 million dollars, is currently so widely used that some estimates say that one takes off or lands somewhere in the world every five seconds. The Boeing 747, a four-engine commercial jet capable of carrying over 400 passengers in a nonstop flight from Tokyo to New York City, costs \$250 million dollars to construct. So why does the United States government consider it worthwhile to invest over \$2 billion dollars in one slow airplane with hardly any commercial use?

While cynics might snicker at the idea of logical government investments, the money supports the development of the future generation of stealth bombers. The Northrop-Grumman B-2 Spirit is a stealth bomber that looks about the same as a football on radar, making it nearly invisible to enemies and consequently a great asset in air warfare and surveillance. The United States government, the Jet Propulsion Laboratory (JPL), and many

other organizations are eager to support research to further stealth technology.

Because radar uses reflected electromagnetic waves to determine locations and speeds of moving aircraft, knowing precisely how the scattering of waves is governed can provide vital information for navigation and detection. While we know that the reflection of electromagnetic waves is governed by Maxwell's equations, the exact nature of wave behavior at the aircraft surface is an extremely difficult and complex issue. The success of stealth bombers at avoiding detection is dependent on new technology developed to thwart the scattering of these waves.

Behavior such as that found on the air-surface interface is only one of the numerous physical surface phenomena that can be described by differential equations. Subsequent application of higher-order accurate algorithms to solve them is advantageous in a large number of fields, including aircraft design, biological modeling, graphics, fluid mechanics, and applied mathematics. Mathematical modeling of surfaces and the phenomena that occur at surfaces is currently one of the most helpful tools in resolving exactly what is happening at a given interface.

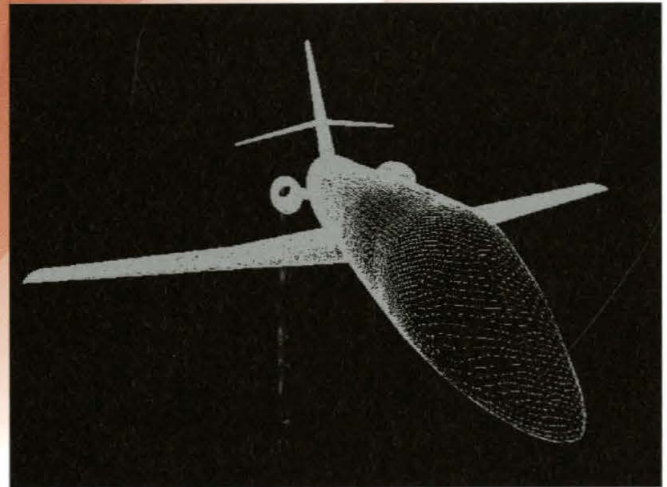


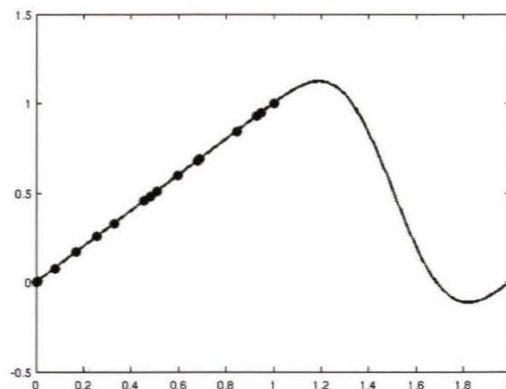
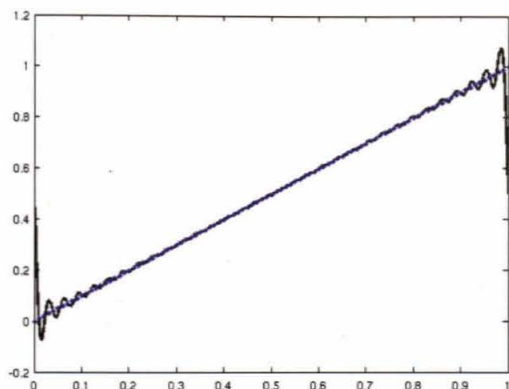
Figure 1. Triangulated Airplane Employing the technique of triangulation, the airplane can be represented as a surface entirely composed of triangles. The aim of the research is to convert this simplistic representation into an accurate surface representation.

Common Methods of Surface Modeling

To solve the governing differential equations with high accuracy, it is critical to be able to represent the surfaces (where boundary conditions are enforced) with high accuracy as well. Thus, in order to accurately predict the interactions of fields or fluids near surfaces, several steps must be taken in order to first numerically represent the surfaces. Other algorithms that are not the focus of this research are subsequently used to solve the differential equations.

First, a three dimensional representation of the surface must be produced. Surface data points are often produced by means of Computer Aided Design (CAD) software, which may render surfaces in a variety of formats such as surface triangulations. [Figure 1]. A triangulation approximates the surface by expressing each data point as a vertex of a few small triangles. Unfortunately, this is inappropriate for input into the necessary high-order algorithms because it is a very crude approximation of the surface.

Figure 2. Gibb's Phenomenon These two plots show the improved approximation made by Fourier Series near boundaries using the continuation method. In both the blue line is an arbitrary linear function of x , and the black curve is an approximation of the blue line's function.



(a) The blue line is fit using a Fourier Series over the domain $[0,1]$, but there is clearly larger errors near the boundaries that do not improve significantly with more terms. (b) The same blue line segment is present with an extended domain. The black curve approximation is extended into a larger domain via the continuation method. The result is a very accurate fit of the line over the domain of interest, $[0,1]$.

The most common method for modeling these surfaces is generally known as freeform surface modeling. The surfaces are from a family of curves called splines, which are composed of a series of polynomials similar to Taylor series. Splines are defined by their control points, which in the case of triangulation are the vertices of the triangles. The spline surface does not necessarily pass through each control point, but each control point influences the surface shape. It can be imagined as having springs connect each control point to the surface to pull the surface towards it and adapt the proper curvature. In this way, the spline surface fits the data of the given surface reasonably well. This method is used extensively in engineering, particularly in computer aided design software (CAD), but it lacks in accuracy. A fundamental problem with this method is that it requires too many terms to achieve the convergence needed for our desired accuracy levels.

Continuation Method of Surface Modeling

Other methods have been developed to produce a more precise three dimensional representation of surfaces at varying levels of accuracy and speed. Dr. Bruno's group at the California Institute of Technology has recently developed an algorithm based on the continuation method for a fast and accurate method.

As an overview, the points are first partitioned into different regions, a previously manual procedure. For example, in the case of an airplane, the nose, wing, and fuselage might be taken as different regions. For each region, a parameterization is chosen so each point can then be identified by both the original

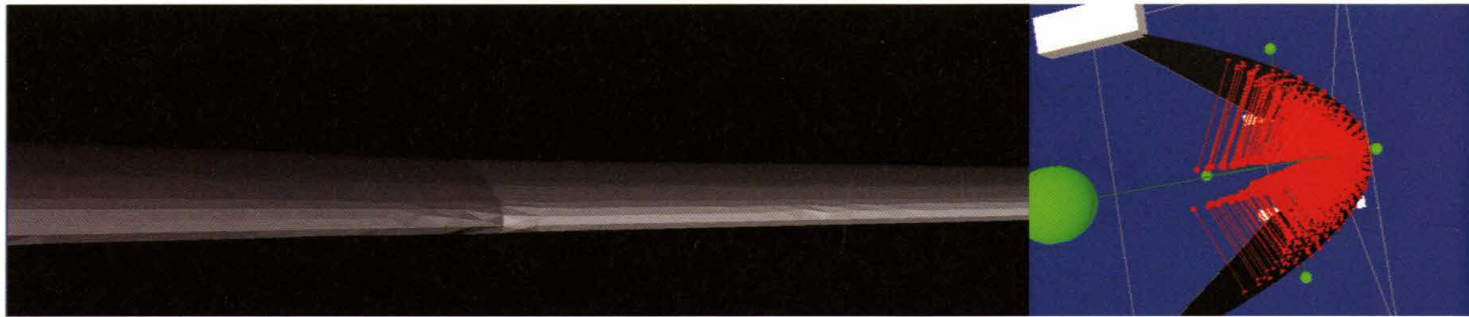
coordinates and the new parametric coordinates. For each region, these coordinates are passed as input to an algorithm implementing the continuation method, and it finds a surface which fits these points to high-order accuracy. Then the surfaces are pieced together to form the entire surface, accounting for corners, discontinuities, and singularities.

Fourier series, rather than series of polynomials, are exploited in Dr. Bruno group's algorithm. Fourier series comprise sine and cosine terms of differing amplitudes and periods that can be used to approximate a given curve. While it is relatively simple to find the Fourier series of a closed-form set of equations such as an explicit function, the same analysis with discrete points is a more difficult task (not to be confused with the Discrete Fourier Transform, which transforms points to the frequency domain). The continuation method fits Fourier series to discrete points.

Another common problem with using Fourier series in surface modeling algorithms is an issue called the Gibb's phenomenon. The Gibb's Phenomenon comes from the inability of the sinusoidal terms of the Fourier series to fit discontinuities at the edge of the domain or surface. Consequently, the edges of the fit are likely to be poorly approximated. The continuation method developed by Dr. Bruno's group solves this problem by extending the domain of the function and defining the function over it in a repeating manner [Figure 2]. Because this makes the function periodic, the Gibb's Phenomenon is essentially eliminated over the domain of interest.

Figure 3. Wing Projected onto Paraboloid

(a) A triangulation of an aircraft wing. (b) Every red dot inside the black paraboloid is an xyz-data-point on the wing of the airplane. Each is projected onto the paraboloid, following the red lines. These points are also shown in red on the black paraboloid. The image is taken from *fasstViewer*. (c) This shows the uv-surface paraboloid from (a) flattened. Each red point has uv-coordinates, and the uv-plane is shown. The denser region in the middle corresponds to the larger number of points near the leading edge of the wing and the base of paraboloid. (d) After the projection and the continuation method are applied, the result is this explicitly defined surface representing the wing to high-order accuracy.



(a)

(b)

However, before a Fourier representation and the continuation method can be employed, the three-dimensional points in xyz-space must first be mapped smoothly to a two dimensional uv-space [Figure 3]. In other words, the coordinates of the three-dimensional surface must be parameterized into a two-dimensional representation labeled with the axes u and v . Given this information, the continuation method can be used to return an explicit surface in three dimensional space in the form of a finite Fourier series with high-order accuracy.

Manipulation and Parametrization of Surfaces

The data points must be mapped from three to two dimensions. The two-dimensional uv-space is formed by drawing a line from every point, or every vertex of every triangle, that is normal to a chosen uv-surface. The uv-surface must be selected carefully to best complement the surface being modeled to ensure minimal loss of accuracy. In addition, the corresponding points on the uv-surface must be as evenly distributed as possible without distorting the original points' spacing. This method is similar to geographic map projections in which the uv-surface is the map and the xyz-points are uniformly scattered on a globe. The goal is to make an accurate yet easily analyzed two-dimensional map.

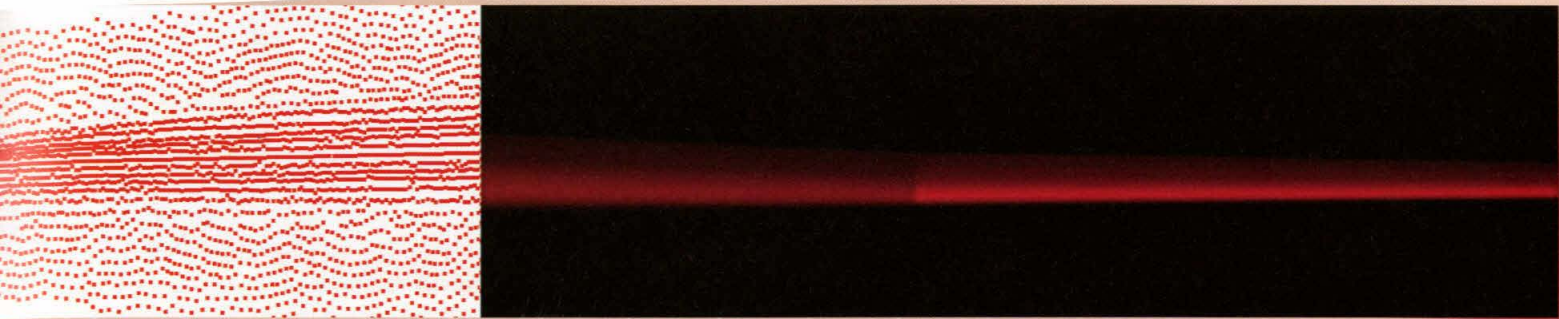
Mathematically, the projection of a globe to a map has minimal distortion if the Jacobian is relatively constant. The Jacobian is a measure of the stretch of an infinitesimal area from the original coordinate system to the area in the new coordinate system. Producing a complicated map with many cuts makes the distribution of points uniform, which is related to a good Jacobian; however, it is difficult to read and define mathematically. While a basic square map is easily read and defined, the

points are distorted and not uniform making the map inaccurate and have a poor Jacobian. Accuracy of the calculations depends on the proper choice of uv-surfaces. To ensure that the mapping satisfies requirements such as one-to-oneness—the property that a data point maps to a unique point on the uv-surface and vice-versa – and a nearly constant Jacobian, the object is divided into subsections that are more simply mapped to geometric shapes.

After the projection of the surface to two dimensions, the three-dimensional surface is computed using the continuation method using the five coordinates (u, v, x, y, z) of each data point. Using the resulting surface representation, we use the continuation method to obtain a number of explicit Fourier series, each one of which represents large portions of the given surface. (The continuation method in itself is not the focus of this work.).

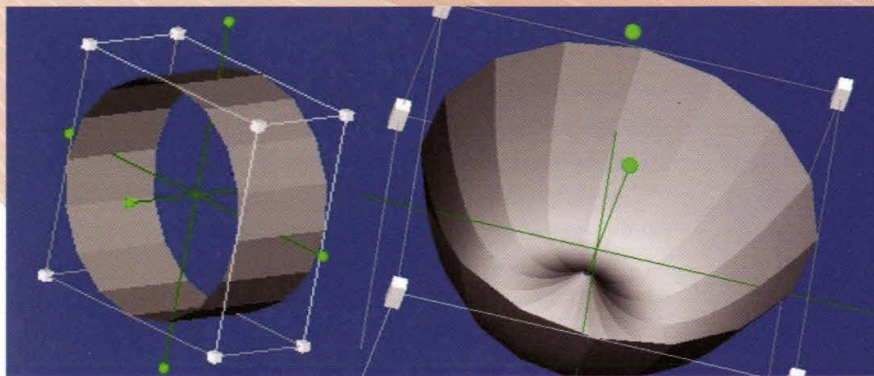
***fasstViewer*: Automation of Surface Modeling**

Taking a step back and looking at this procedure from a practical standpoint, changing the form of the data from points to surfaces can be both tedious and inaccurate. First, the uv-surface must be oriented optimally to obtain a meaningful mapping of the data points. *fasstViewer*, a computationally efficient geometric interactive graphics program written in C++ using an open source graphics package (Coin3D), was developed to orient the surface, and, moreover, to automate the entire process. In its early stages, *fasstViewer* allowed the human user to graphically see the data points, orient the camera, place and manipulate simple uv-surfaces, and project the data points to the uv-surface analytically. The final goal for *fasstViewer* is to require almost no user input.



(c)

(d)

**(left) Figure 4. Cylinder UV-Surface**

The cylinder uv-surface is shown as represented in fasstViewer. It allows for more data-point geometries to be mapped from xyz to uv coordinates with minimal distortion. In the example of the airplane surface, it can be used for the outside of engine intake and the main fuselage.

(right) Figure 5. Paraboloid-on-a-circle UV-Surface

The paraboloid-on-a-circle uv-parameterized projection surface is shown as represented in fasstViewer. In the example of the airplane, this uv-surface is especially well-suited for projection of the nose cone as well as the leading edge of engine intake (as seen in Figure 6). The blue points are xyz-data-points. The white and green handles allow the user to adjust the size and rotation of the shape.

To provide greater detail of the process, one of the focuses in Dr. Bruno's group is the evaluation of the reflection of acoustic and electromagnetic waves off the surface of an airplane. The behavior of these waves is governed by the Helmholtz equation for acoustic scattering as well as the Maxwell equation for electromagnetic scattering. While these equations may be solved in a variety of ways, one is through use of the high-order numerical algorithms developed in Dr. Bruno's group.

Additional Functionality

We made notable advances towards automating fasstViewer. The first was the addition of new uv-surfaces. For fasstViewer to be useful, it must have all of the uv-surface shapes necessary to completely map any complex surface to uv-space. Using an airplane as an example, the addition of two more shapes, a cylinder [Figure 4] and a paraboloid-on-a-circle [Figure 5], ensures that any correctly chosen part of the airplane can be projected onto uv-space with minimal distortion.

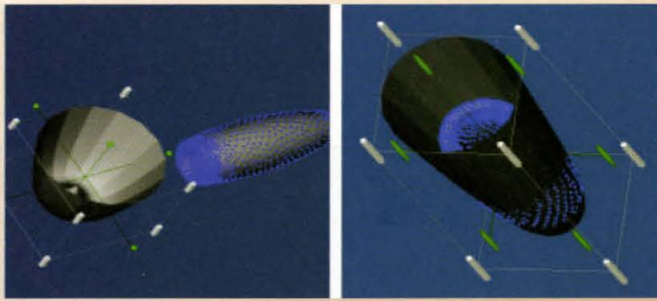


Figure 6. Engine Intake Projected onto Paraboloid-on-a-circle
 (a) A paraboloid-on-a-circle projection surface next to the engine intake with data-points shown in blue. The two are completely unaligned.
 (b) After calling the rough alignment function on the data in (a) the projection surface has been stretched and aligned with the data-points of the engine intake.

For fasstViewer to automatically return an airplane composed of smooth surfaces, it is necessary to align uv-surfaces with a set of data points without user input [Figure 6]. This is a two step process; fasstViewer first roughly places the uv-surface with correct dimensions, orientation, and other parameters around the data points. The application then optimizes the alignment for a more accurate projection to uv-space. Using a statistical approach (Principal Component Analysis), the dimension with the most variation, second most, and least are discovered. Analysis of these dimensions determines whether the uv-surface is well-oriented for the particular data set. The second step of optimizing the alignment is more difficult and is discussed in more depth later.

After a uv-surface is aligned properly, the data points are projected onto it. Analytically projecting is often difficult; therefore, a fast, robust, reliable, and accurate numeric solver was developed to find the projection for any uv-surface. First, an initial guess of sample points on the uv-plane is created and every data point in xyz-space is matched to its closest sample point. Then minimizing the absolute value of the dot product of the projection line with the normal of the uv-surface yields the optimal result. The ability to numerically project is extremely valuable for any future shapes implemented because the most complex and vital portion is already completed.

Current Status Report

Recently fasstViewer has been upgraded substantially. With a new GUI, many steps are entirely automated. The user selects the section of the airplane to be projected, and one of the sev-

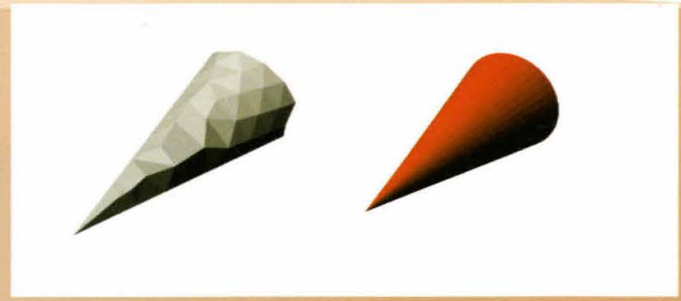


Figure 7. Example of Finished Tail Tip (Using the original GUI)
 (a) This is an example of a given triangulation of the tail tip. The data-points are the intersections of each triangular panel. It is clear that this is a very poor approximation of a true tail tip on an airplane.
 (b) After calling various fasstViewer functions, the tail tip is transformed from a triangulation to an accurate surface representation of the true nose cone. Repeating this process on each part of the airplane results in the full surface representation.

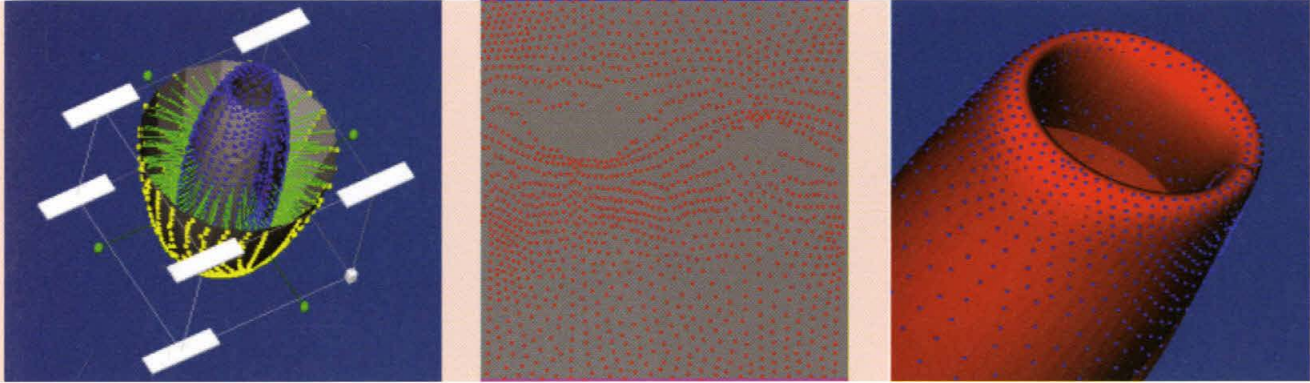
eral uv-surface shapes. After that, this new version aligns the uv-surface with the data points, optimizes this alignment, and projects entirely automatically. The option to manually do each of these steps still exists as well. Then, using the powerful algorithms developed by Dr. Bruno's group, fasstViewer runs code for the continuation method which accurately fits a surface to the points using the uv- and xyz-data, and then displays the result. The finished product is a surface that, to a high order of accuracy, fits the original triangulated airplane segment [Figure 7]. Completing the entire airplane is simply a matter of repeating the process on each segment [Figure 8] [Figure 9].

Future Work

In the future, the ability to automatically break the airplane into pieces so they can be projected onto a uv-surface will be developed, but this is not a straight-forward process. The human eye naturally differentiates parts of the airplane. However, as is a recurring theme throughout this research, expressing a human's intuition mathematically requires keen insights if it is to be accomplished in a general, reliable, and robust way.

Some work has been done on automating this process, but it can be furthered. It eliminates the need for the user to manually sort the data set and project to different uv-surface shapes, tasks which are time-consuming and difficult. At the focus of this is creating an objective function, a way of assigning a score to a different subsets of data points and how well they project onto a particular uv-surface shape, that takes into account all of the relevant characteristics. A major complication is local minima preventing a minimization routine from converging to

Figure 8. Example of Finished Engine Intake (Using the original GUI)



(a) This shows the uv-surface aligned and the xyz-points projected onto it. The refining of the alignment was done by hand. The projection surface is a paraboloid-on-a-circle. The blue points are xyz-data-points and the yellow lines show how they project to uv-space.

(b) The uv-plane corresponding to (a). It is also worth noting how the uv-plane is fairly uniformly filled with points, as desired. The missing section comes from part of the engine intake not having any data-points and is expected.

(c) An example of a finished piece. The red surface fits the blue points extremely accurately.

the absolute minima of the scoring function.

Another obstacle is the computation time required for such a function. If it is not done properly, it could take hours rather than seconds. There has been a sizeable amount of research on this topic and while good algorithms exist, none exactly matches the needs of fasstViewer. Dr. Bruno's group is working to overcome this, and the other, difficulties.

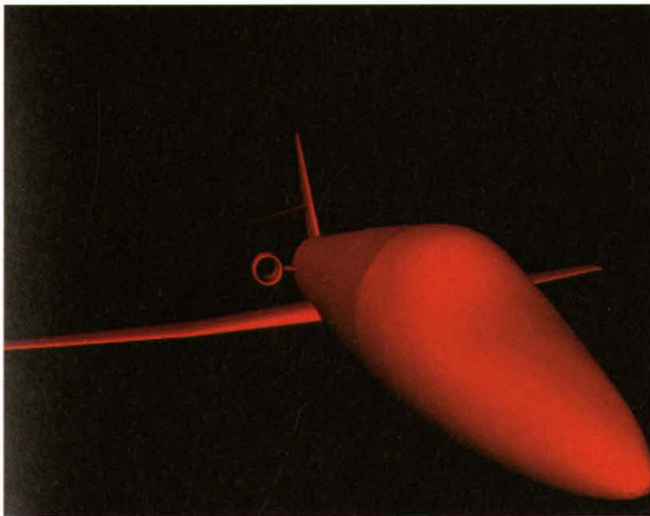


Figure 9. Finished Airplane

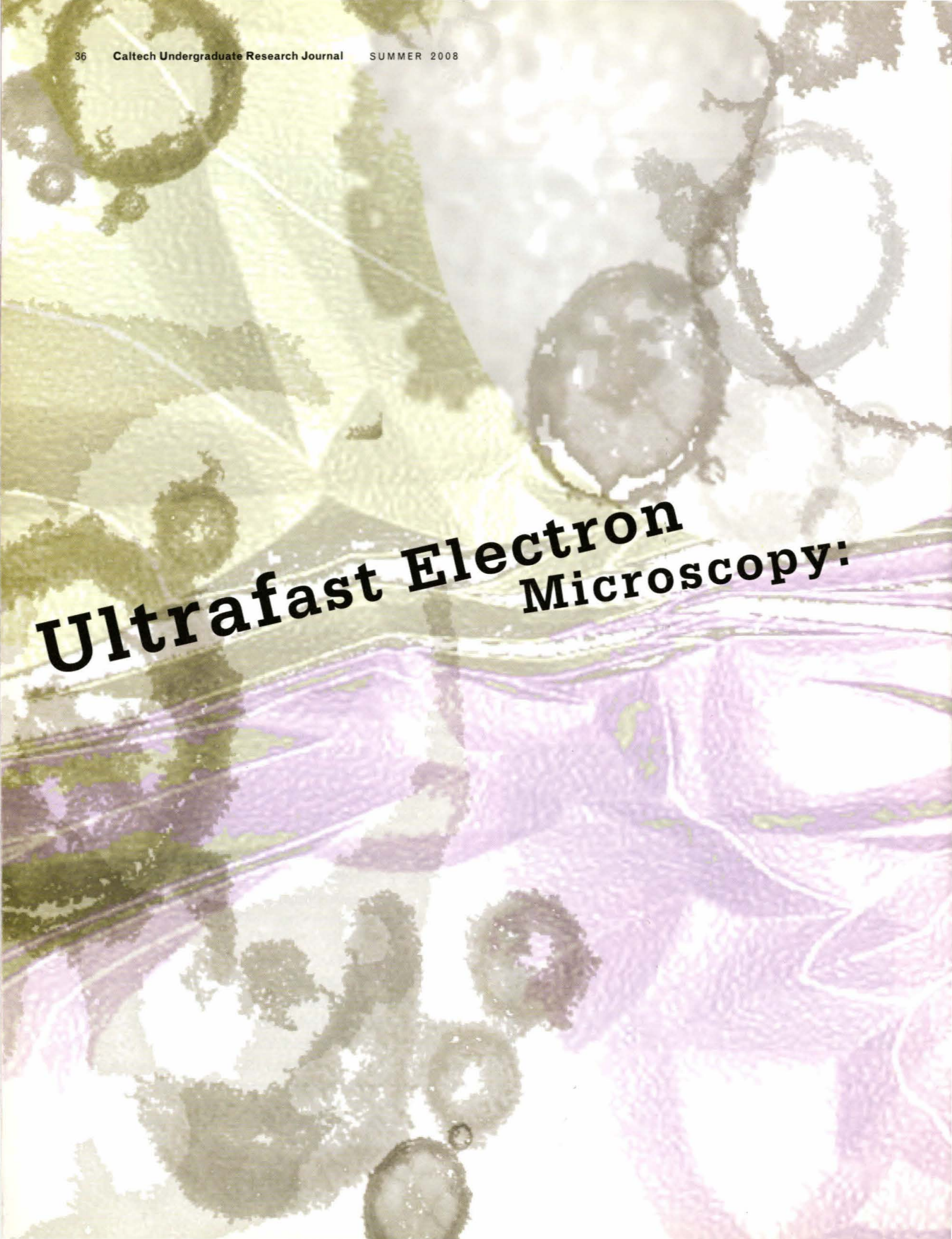
To achieve this image, each section of the airplane is separately projected onto uv-surfaces. This information is passed to an algorithm implementing the continuation method, which produces the surface. These sections are then combined by matching each of the boundaries.

Further Reading:

- [1] Bruno, Oscar P. "Fast, High-Order, High-Frequency Integral Methods for Computational Acoustics and Electromagnetics." Topics in Computational Wave Propagation Direct and Inverse Problems Series Lecture Notes in Computational Science and Engineering, Vol. 31 Ainsworth, M.; Davies, P.; Duncan, D.; Martin, P.; Rynne, B. (Editors.)
- [2] Bruno, Oscar P. et al., "Accurate, high-order representation of complex three-dimensional surfaces via Fourier continuation analysis." Journal of Computational Physics 227 (2007) 10941125doi:10.1016/j.jcp.2007.08.029
- [3] Press, W., Teukolsky, S., Vetterling, W., and Flannery, B. Numerical Recipes in C. 1992
- [4] Meyer, M, Desbrun M, and Alliez, P. "Intrinsic Parameterizations of Surface Meshes." Eurographics 2.21 (2002)
- [5] Floater, M. S. Parameterization and Smooth Approximation of Surface Triangulations. Computer Aided Geometric Design 14. 3 (1997): 231-250. ISSN 0167-8396

Acknowledgements:

I thank Oscar Bruno for guidance in this project. I also thank Randy Paffenroth, and Tim Elling for their vital assistance. This project was funded by a grant from the Jet Propulsion Laboratory (JPL), the California Institute of Technology Summer Undergraduate Research Fellowship (SURF) program, and Mr. and Mrs. Robert Noland who sponsored my SURF.

A high-magnification electron micrograph of a cell. The image shows various organelles, including a large nucleus with a prominent nucleolus in the upper right. The cytoplasm is filled with a complex network of membranes and organelles. The image is colorized, with purple highlighting certain membrane structures and green highlighting others. The overall appearance is that of a detailed biological structure.

Ultrafast Electron Microscopy:



Watching Atoms Move and Crystals Melt

Garrett K. Drayna and David J. Flannigan
Mentor: Ahmed H. Zewail

Introduction

Imagine being able to actually watch the atoms move inside a grain of salt, or being able to see how ions are transported across the hydrophobic cell membrane.

In order to do this, you would need a completely new type of methodology. This technique would have to be able to combine the very high spatial resolution necessary to actually see atoms (on the order of one angstrom, where one angstrom = 10^{-10} meter) with the high temporal resolution necessary to see those atoms move (on the order of a femtosecond, where one femtosecond = 10^{-15} second). For decades, researchers have relied on static images provided by electron microscopy and static diffraction patterns provided by X-ray crystallography to infer how a system operates. The major drawback to these otherwise very powerful techniques is that no direct experimental evidence is gathered about the structure of the transition states of the system. That is, these techniques can only provide information about the three spatial dimensions; while information about how the system behaves in the fourth dimension – time – remains a mystery. Therefore, to overcome this fundamental problem, a methodology that can access all four dimensions simultaneously must be realized and demonstrated. The development of such a technology would mark a great day in the advancement of human knowledge. Fortunately, that day has arrived with the advent of Ultrafast Electron Microscopy (UEM).

Ultrafast Electron Microscopy

In the Physical Biology Center for Ultrafast Science and Technology (UST) at Caltech, a revolutionary new method of microscopy has been developed that makes the direct observation of the smallest, fastest, and most complicated processes feasible. This new methodology is called Ultrafast Electron Microscopy because of its ability to access the fourth dimension – time – in addition to the three spatial dimensions. Essentially, UEM combines the well-established sub-nanometer (nanometer = 10^{-9} meter) spatial resolution of a standard transmission electron microscope (TEM) with the femtosecond time resolution of an ultrafast laser system. By providing access to these spatial and temporal domains, the direct visualization of the structural dynamics of matter on the atomic-scale and on the time-scale of molecular bond vibrations is now within reach.

The UEM methodology is based upon the stroboscopic pump-probe technique. The main difference between the well-established spectroscopic pump-probe techniques and UEM is that electrons, rather than photons, are used to probe the excited sample. The use of electrons as probes allows for analysis of the actual atomic-scale structural changes induced by the pump laser pulse, because of the much shorter wavelength of fast electrons relative to optical photons from the de Broglie relation. The laser system used for the first-generation UEM, known as UEM1, consists of a diode-pumped, mode-locked Ti:sapphire oscillator, which generates 120 fs pulses of 776 nm laser light with a repetition rate of 80 MHz and an average power of three watts. The repetition rate can be varied by placing an acousto-optic pulse picker in the optical axis. The beam is split into two arms: one that is frequency-doubled to generate near-ultraviolet light, while the other serves as the pump laser and is directed into the UEM column and focused onto the sample. The pulses in the near-ultraviolet arm travel through a variable time delay line and then to a photocathode, which is also housed in the UEM column. Irradiation of the photocathode with near-ultraviolet laser light generates packets of electrons, which are accelerated to 120 keV and probe the photoexcited sample. A conceptual diagram of the UEM technique is shown in Figure 1.

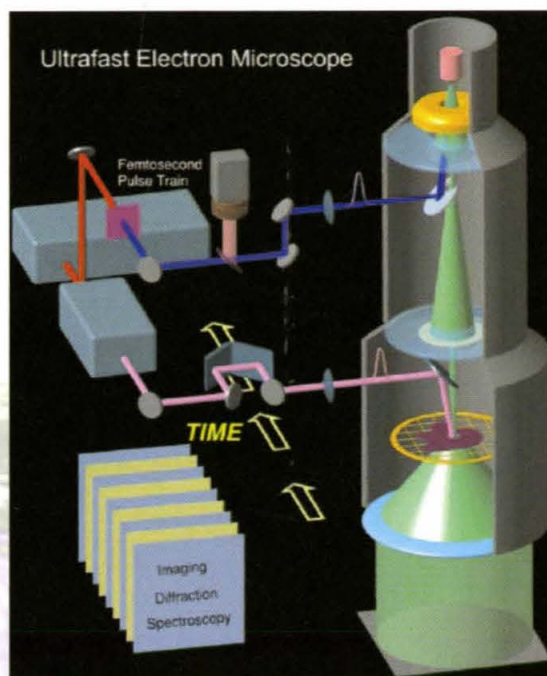


Figure 1. The ultrafast electron microscope. The setup involves interfacing a TEM with a train of femtosecond optical pulses to generate an electron beam in ultrafast packets of as few as one electron per pulse. The other optical beam delivers, after a time delay, initiating pulses at the specimen. Other critical components include the microscope lens system, charge-coupled device camera, and image acquisition and processing software. Figure adapted from Lobastov, V. A. *et al. Proc. Natl. Acad. Sci. U.S.A.* **2005**, *102*, 7069.

As previously mentioned, the UEM is used to resolve structural dynamics via a stroboscopic method because of the very low number of electrons in each probe pulse. Having only a few electrons per packet allows for Coulombic space-charge broadening to be avoided; this broadening would limit temporal resolution due to the increased spread in arrival time of the electrons at the sample. Because each packet contains only a few electrons, an image is not formed after only one pulse due to the

small number of total interactions with the sample. Therefore, to build up a single image the use of several pulses is necessary. Once an image of the sample at a certain time delay is obtained, the time difference between the pump and probe beams is increased and the process is repeated. By changing the time delay between the pump and probe pulses, a series of images can be obtained that are representative of the ultrafast structural dynamics of the material being studied. These images can then be linked together to form a movie of the dynamics under study. In addition to UEM1, which operates at 120 kV, UST at Caltech recently developed the second generation UEM, UEM2, which operates at 200 kV. In addition to electron diffraction and imaging, UEM2 can also operate in a scanning mode (STEM) and is capable of measuring electron energy loss spectra (EELS). The ability of the UEM methodology to reach similar spatial resolutions of a standard TEM is illustrated in Figure 2.

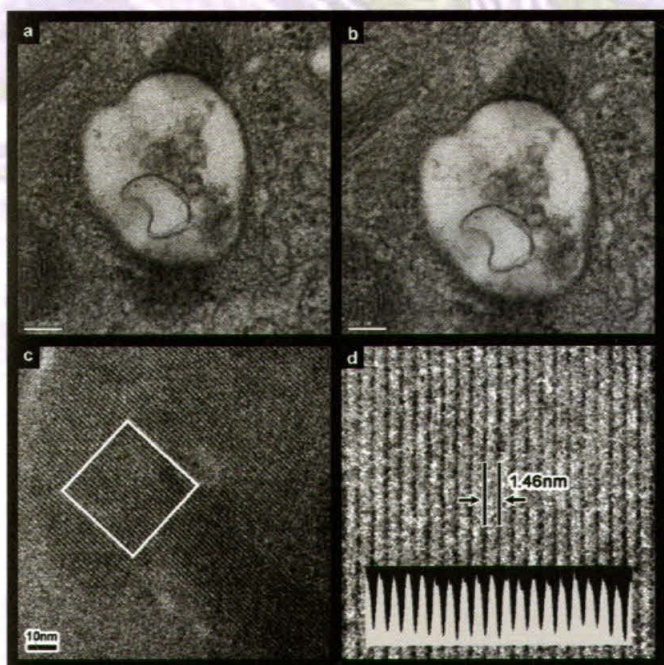


Figure 2. Can you tell the difference?

(a) UEM and (b) corresponding TEM image of a vesicle inside a positively stained rat intestinal cell. The scale bar in the lower left corner of the images represents 100 nm. (c) High-resolution UEM image of a crystal of chlorinated copper phthalocyanine showing the crystal lattice fringes. (d) Magnification of the selected area shown in (c) revealing the 1.46 nm spacing between the copper planes. Panels (a) and (b) adapted from Lobastov, V. A. *et al. Proc. Natl. Acad. Sci. U.S.A.* **2005**, *102*, 7069. Panels (c) and (d) adapted from Park, H. S. *et al. Nano Lett.* **2007**, *7*, 2545.

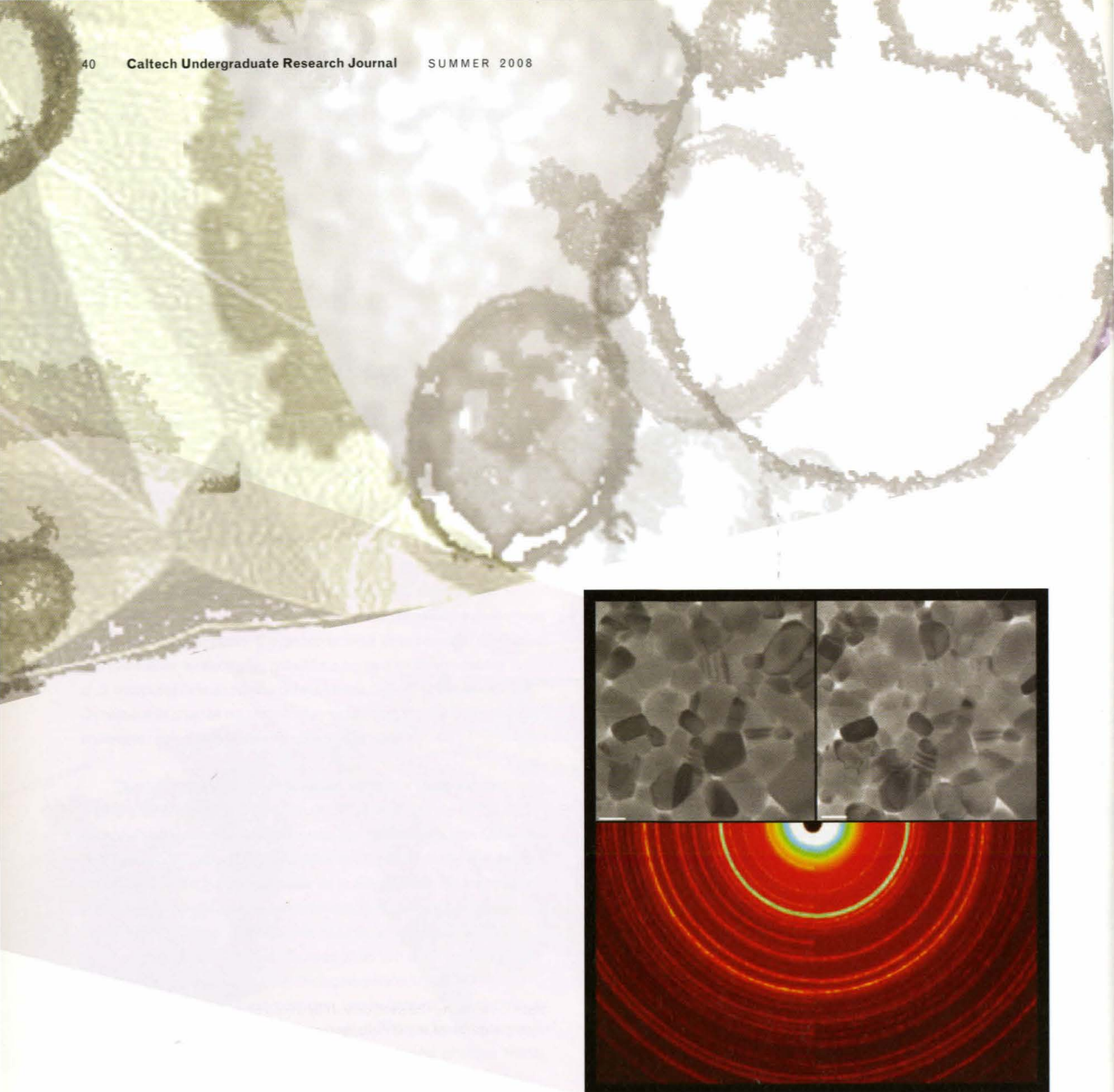


Figure 3. The upper two panels show UEM images of the same region of a polycrystalline VO₂ film obtained before (Left) and after (Right) the laser-induced phase transition. The white scale bar shown in the lower left corner of each figure represents 100 nm. The lower panel shows the composite experimentally observed diffraction patterns from each of the films shown in the upper panels. The diffraction patterns clearly show the change in the ring pattern arising from the change in unit cell symmetry that occurs during the ultrafast phase transition. Figure adapted from Grinolds, M. S. *et al. Proc. Natl. Acad. Sci. U.S.A.* **2006**, *103*, 18427.

Resolving Nanoscale Mechanical Motion with UEM

One of the first studies done using UEM was on the structural dynamics of the insulator-to-metal phase transition in vanadium dioxide (VO_2). From previous work, it was known that VO_2 made this transition on an ultrafast time-scale, making it an ideal candidate for study with the new UEM system. The results were nothing short of spectacular. Not only was a detailed profile of the structural phase transition on the sub-picosecond timescale (picosecond = 10^{-12} second) elucidated in diffraction mode, corresponding real-space images revealed striking changes in contrast within crystalline VO_2 domains (Figure 3).

More recently, UEM has been used to discover previously unknown photoinduced mechanical motions in an otherwise well-characterized metal-organic molecular material, copper 7,7,8,8-tetracyanoquinodimethane (Cu-TCNQ). This material belongs to a large class of charge-transfer complexes known as quasi one-dimensional molecular semiconductors. Many of these materials have phase transitions known as spin-Peierls transitions, which occur as a result of the separation of spin-paired electrons located on neighboring TCNQ radical anions. The separation of the paired electrons results in an ultrafast movement of stacked TCNQ molecules away from one another but only along one of the three crystallographic axes. This phase transition can be initiated by near-infrared laser light.

To observe these dynamics, single crystals of Cu-TCNQ ranging in size from several micrometers to tens of nanometers were synthesized directly on the surface of an amorphous silicon nitride (Si_3N_4) film that was 50 nm thick. What was observed with UEM was striking and would not have been possible with a conventional TEM. After fracturing a single crystal with laser pulses, it was discovered that the crystals would expand preferentially along one crystallographic axis when exposed to laser light. When the laser light was blocked, the crystal would return to its original structural configuration. By pulsing the laser repeatedly, it was shown that this expansion and contraction

was robust over many cycles (Figure 4). Analysis of the crystal lattice spacing as a function of laser fluence confirmed that the anisotropic expansion observed on the nanoscale originated from atomic-scale motions.

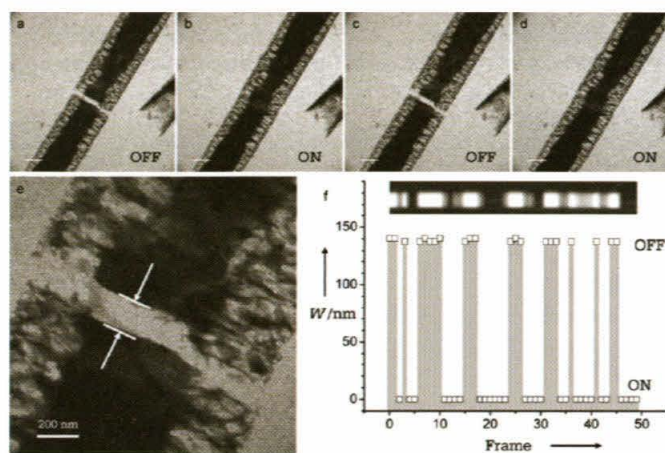


Figure 4. (a – d) UEM images of the expansion and contraction of a Cu-TCNQ single crystal. The sequential views (scale bar = 500 nm) show the fractured single crystal in the “OFF” state (a, c; no pulsed-laser irradiation) and in the “ON” state (b, d; pulsed-laser irradiation). (e) Higher-resolution image of the crystal in the “OFF” state illustrating the section within which quantification of the reproducibility of the expansion/contraction was performed. (f) Plot showing the results of a sequence of “ON” and “OFF” cycles. The channel width (W) varied from 0 (pulsed-laser irradiation) to 140 ± 5 nm (no pulsed-laser irradiation) over a series of 50 frames. The bar above the data points illustrates the modulation in a memory recording. Figure adapted from Flannigan, D. J. *et al. Angew. Chem., Int. Ed. Engl.* **2007**, *46*, 9206.

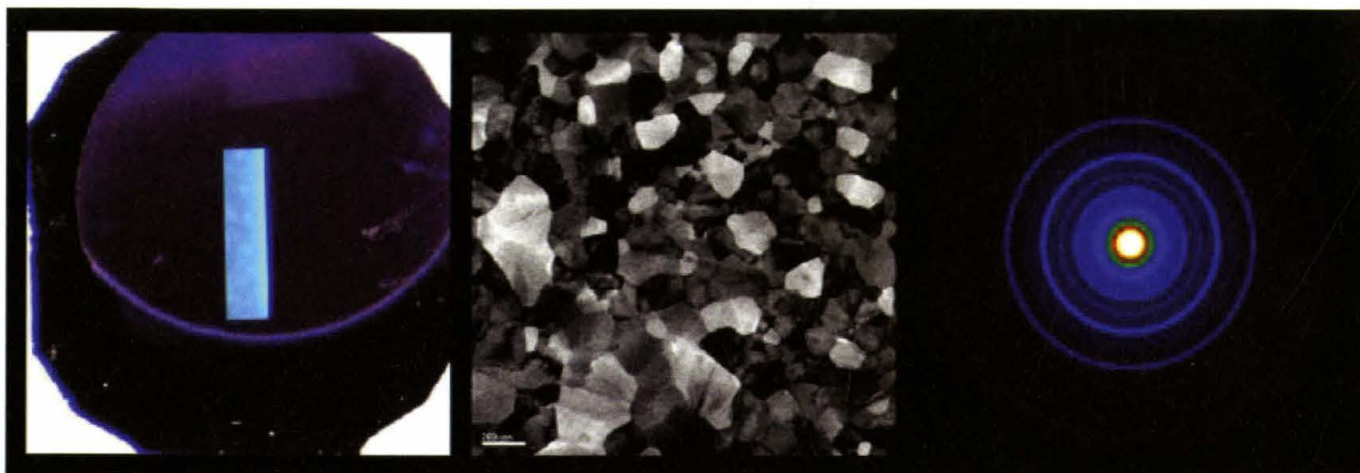


Figure 5. The series of panels show the following: (Far-left) Optical microscope image of a thin K-TCNQ film (blue/purple) deposited onto a Si_3N_4 membrane TEM grid. The light-blue rectangle in the center of the grid is a 2.0×0.5 mm window used for specimen viewing in TEM. (Center)

UEM image of the K-TCNQ polycrystalline film shown in the far-left panel. The scale bar in the lower left corner represents 200 nm. (Far-right) Rotationally-averaged UEM diffraction pattern obtained from the K-TCNQ polycrystalline film shown in the center panel.

Looking to the Future

Another TCNQ charge-transfer complex that has been widely studied is potassium TCNQ (K-TCNQ). Previous femtosecond optical reflectivity studies on K-TCNQ single crystals have indicated that the photoinduced melting of the spin-Peierls phase in this material occurs on the sub-picosecond timescale. While reflectivity studies of this sort are effective at providing indirect evidence of structural changes, the direct observation of the ultrafast motion of molecules in the unit cell requires a different technique. The UEM methodology is well-suited for elucidating this motion.

As is true of all electron microscopy techniques, the preparation of high-quality samples for UEM studies is absolutely critical to the success of the experiments. Because of this, a novel sample preparation method was developed to prepare polycrystalline films of K-TCNQ directly on thin (30 nm) Si_3N_4 membranes. After cleaning the surface of the Si_3N_4 membrane with argon plasma, a thin layer (20 nm) of potassium iodide (KI) is deposited onto the membrane via thermal evaporation. The sample is then placed in a custom-machined holder, which also serves as a TCNQ reagent source, and the entire apparatus is heated to 120°C under a steady flow of dry argon. As the apparatus warms, the TCNQ sublimates and the vapor reacts with the thin KI film to form K-TCNQ (Figure 5). Characterization of

the thin K-TCNQ film with Fourier transform infrared spectroscopy and surface X-ray photoelectron spectroscopy showed that this synthetic methodology produced very pure films of K-TCNQ with no residual iodine. This represents a significant advance in sample quality over previously reported methods for synthesizing thin K-TCNQ films. Now with a robust way to synthesize these films, work is currently focusing on using UEM to directly visualize the photoinduced structural dynamics of this intriguing molecular material.

There is much promise for using UEM to study the structure-dynamics-function relationships present in complex biological systems such as ribosomes and cell membrane channels. Indeed, elucidating how physical forces affect global function of cellular components at the atomic level is a major goal of UST at Caltech. While the TCNQ-based materials currently under investigation are much simpler than most cellular systems, they do represent an increase in complexity over simple metals and metal oxides previously studied, and are held together with the same forces as those present in complex biological structures. Clearly, the knowledge gained by studying these molecular materials with UEM will be invaluable when applying this methodology to more complex biological systems.

Acknowledgments

Garrett Drayna is a second year undergraduate at Caltech. He would like to thank the Gordon and Betty Moore Foundation, the Air Force Office of Scientific Research, and the National Science Foundation all for funding this research, the Caltech Summer Undergraduate Research Fellowship (SURF) Program, and Drs. Vladimir Lobastov and Jonas Weissenrieder for insightful discussion and guidance. He would especially like to thank his mentor, Prof. Ahmed Zewail, and his co-mentor, Dr. David Flannigan, for their inspiration and guidance.

Further Reading

1. Zewail, A. H. 4D Ultrafast Electron Diffraction, Crystallography, and Microscopy. *Annu. Rev. Phys. Chem.* **2006**, *57*, 65-103.
2. Flannigan, D. J.; Lobastov, V. A.; Zewail, A. H. Controlled Nanoscale Mechanical Phenomena Discovered with Ultrafast Electron Microscopy. *Angew. Chem., Int. Ed. Engl.* **2007**, *46*, 9206-9210.
3. Grinolds, M. S.; Lobastov, V. A.; Weissenrieder, J.; Zewail, A. H. Four-Dimensional Ultrafast Electron Microscopy of Phase Transitions. *Proc. Natl. Acad. Sci. U.S.A.* **2006**, *103*, 18427-18431.
4. Baum, P.; Yang, D.-S.; Zewail, A. H. 4D Visualization of Transitional Structures in Phase Transformations by Electron Diffraction. *Science* **2007**, *318*, 788-792.
5. Gedik, N.; Yang, D.-S.; Logvenov, G.; Bozovic, I.; Zewail, A. H. Nonequilibrium Phase Transitions in Cuprates Observed by Ultrafast Electron Crystallography. *Science* **2007**, *316*, 425-429.



Wireless Power in Space

Will Biederman, University of Washington, Space Grant Summer 2007
Yoseph Bar-Cohen, Xiaoqi Bao, Stewart Sherrit, Mircea Badescu
& **Chris Jones**, Jet Propulsion Laboratory, Pasadena

I imagine a future where you can power your cell phone wirelessly, eliminating the need to recharge your phone via an outlet.

On a larger scale, imagine a space craft docked at the International Space Station wirelessly recharging its batteries before setting off on a mission. Current research at the Jet Propulsion Laboratory (JPL) on the wireless transmission of power into metalically isolated areas, or small areas of space surrounded by metal, can soon turn these scenarios into reality. However, beyond the mere convenience of reducing the clutter of power cables, future NASA missions actually will depend on wireless power transmission.

NASA first became aware of this need while preparing for a Mars Sample Return mission. JPL is planning to send a rover to Mars to collect a soil sample that will be returned to Earth in a small capsule. A sensor inside the capsule is needed to monitor the capsule's condition and relay this information to an outside transceiver. Powering this sensor with wires routed through the container would compromise the seal of the capsule. Instead, NASA must be able to both power this sensor and send data wirelessly through the thick metal capsule.

There are currently several methods of wireless power transmission, such as using magnetic induction, lasers, or radio frequencies. However, these methods have low transmission efficiency, limited power transmission, or require a line of sight between a transmitter and a receiver. Furthermore, the wireless transmission of power through metal has further complications. Due to its conductivity, a metallic wall will prohibit the propagation of electromagnetic waves. To remedy this, a novel method of wireless power transmission using ultrasonic vibrations and the piezoelectric effect was developed by the Nondestructive Evaluation and Advanced Actuators Technologies (NDEAA) laboratory at JPL.

Piezoelectricity: sending power via vibrations

Piezoelectricity is the ability of some materials, commonly ceramics, to generate an electric potential when a mechanical stress is applied. Likewise, these materials produce a mechanical stress when an electric field is applied. Piezoelectric materials are used in many common household items, such as in the lighter of a gas grill. The clicking sound you hear when the grill is turned on is from a hammer hitting a piezoelectric material. This in turn produces a high voltage across the spark gap, causing the gas to ignite. By taking advantage of these properties, power can be transmitted wirelessly in the form of stress waves propagating through a metallic wall. This transmission technique is analogous to how whales communicate in water; a whale generates a call in the form of a pressure (acoustic) wave that propagates through a medium (water) and is detected by another whale. Although metal inhibits the transmission of electromagnetic waves, it enables highly efficient propagation of stress waves. These stress waves are technically called acoustic waves, which are defined as a pressure, or stress, change that moves at the speed of sound. Thus, this transmission technique is also known as an acoustic-electric power feed-through.

Using these properties and techniques, we can theoretically transmit power through any metallic wall. To demonstrate this concept, a device for power transmission can be fabricated by sandwiching a metal disc between two piezoelectric materials [Figure 1]. When voltage is applied at a certain frequency to the "transmitting" piezoelectric material, the material will produce vibrations (mechanical stress) at the same frequency. These vibrations then travel through the metal disc and cause the "receiving" piezoelectric to distort and produce a voltage with the same frequency.

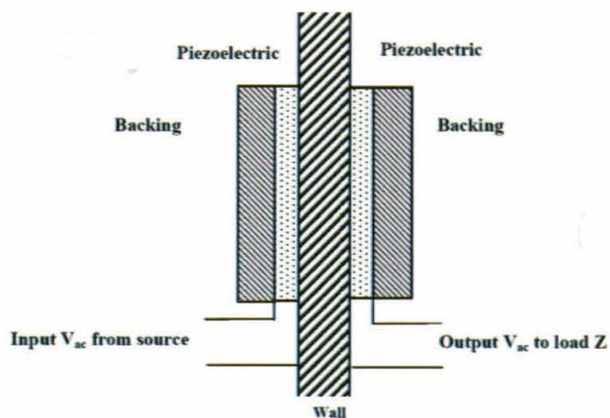


Figure 1. Principle of an acoustic electric transmission device, with piezoelectric transmitter and receiver

Designing a 1 kW wireless power transmission device

In 2006, a prototype device was developed and capable of transmitting 100 W at 87-88% efficiency through a 3.4 mm thick titanium plate using two ceramic disk piezoelectric transducers. In order to increase the power transmission to 1000 W, it was necessary to enhance and optimize the original device. The level of stress necessary to produce power at the 1000 W level in piezoelectric ceramics, however, would exceed the maximum amount of stress that can be applied to the material before it fractures.

In order to resolve this, the number of piezoelectric disks was increased from two to four, which allows a greater electrical current to be transmitted for the same voltage (thereby increasing the power). Since the compressive strength of ceramics is much larger than the tensile strength, the piezoelectric disks were pre-stressed under compression using a stress bolt to prevent fracturing.

A prototype transmittance device consisting of two identical piezoelectric stacks is shown in Figure 2. Each stack consists of four individual piezoelectric ceramic disks that are 38 mm in diameter and bonded together by epoxy. As the device is symmetric about its center, either stack may serve as the power transmitter or the receiver. To reduce the fabrication costs for this prototype, the titanium plate was kept to a diameter of 85 mm. This small diameter means that the radial surface waves (Lamb waves) in the plate generated from the vibrations are not dissipated and are instead reflected when they reach the edge of the plate. Therefore, for this prototype we will not suffer from significant acoustic loss, which will be a realistic problem in large-scale implementation. Unfortunately, the small surface area of the plate also leads to heat buildup and limits the time we can operate the device. Plates with larger surface areas can dissipate heat more efficiently, but they do not perform as well due to acoustic leakage in the form of Lamb waves in the plate.

To evaluate the utility of this device for transmitting power using acoustic waves, an experimental setup [Figure 3] was designed and built to measure the power transmissions and the power transfer efficiency. We define the power transfer efficiency as the power delivered to a load divided by the input power. The input power was generated from amplified signal generators applied across the input electrodes of the device. On the receiving end, we connected a load resistance across the output electrodes to simulate the resistance of the device that we are trying to transmit power to, such as light bulbs. To measure the input and output power, a multi channel digital oscilloscope was used. The input and output voltages are measured using high voltage probes, and the input current was measured using a current

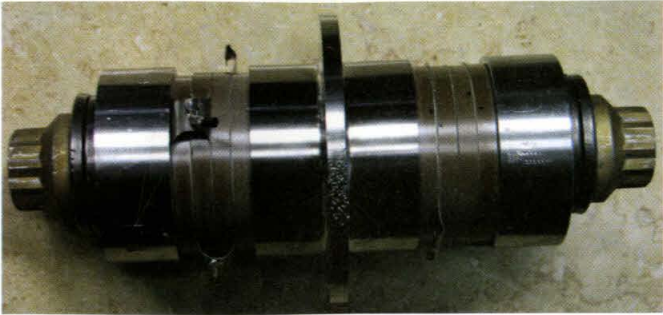


Figure 2. The developed transmission device with a pair of piezoelectric stacks

probe. Using these measurements, the average input power to the device as well as the output power was calculated. The formulas used to calculate the input power, output power, and transfer efficiency are presented in Figure 3.

To evaluate the utility of this device for transmitting power using acoustic waves, an experimental setup [Figure 3] was designed and built to measure the power transmissions and the power transfer efficiency. We define the power transfer efficiency as the power delivered to a load divided by the input power. The input power was generated from amplified signal generators applied across the input electrodes of the device. On the receiving end, we connected a load resistance across the output electrodes to simulate the resistance of the device that we are trying to transmit power to, such as light bulbs. To measure the input and output power, a multi channel digital oscilloscope was used. The input and output voltages are measured using high voltage probes, and the input current was measured using a current probe. Using these measurements, the average input power to the device as well as the output power was calculated. The formulas used to calculate the input power, output power, and transfer efficiency are presented in Figure 3.

Preliminary testing

We used an automated LabView program to sweep a signal generator through a broad range of frequencies. Analysis of the data revealed multiple resonance frequencies of the device where the input impedance was at a minimum and the current was at a maximum. The most efficient resonance frequency was at 24.5 kHz, as determined by applying the formula shown in Figure 3. After running preliminary tests on the device, we

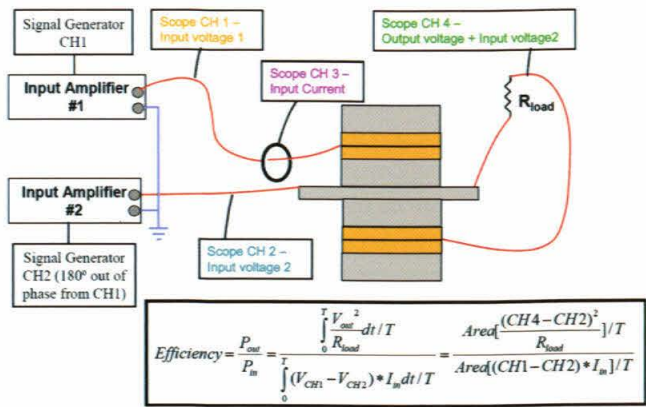
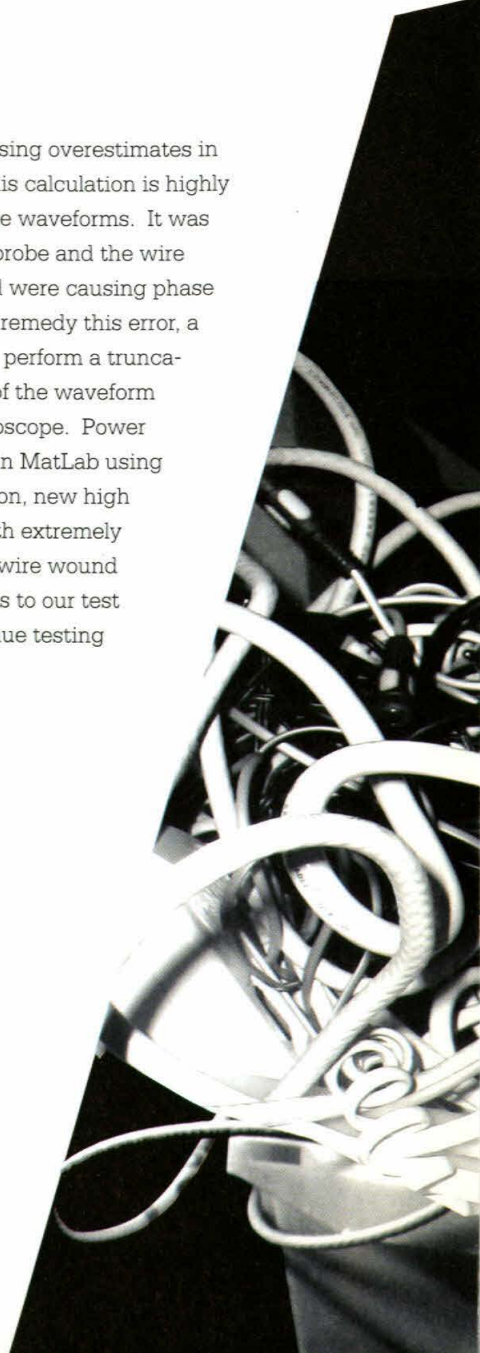


Figure 3. Test bench setup and power calculations

found that our setup was causing overestimates in the efficiency calculation. This calculation is highly dependent on the phase of the waveforms. It was determined that the current probe and the wire wound load resistors we used were causing phase errors in our calculations. To remedy this error, a MatLab script was written to perform a truncation and manual phase shift of the waveform data gathered from the oscilloscope. Power calculations were then done in MatLab using this corrected data. In addition, new high power metal film resistors with extremely low inductance replaced the wire wound resistors. After these changes to our test setup, we were able to continue testing and record our final data.



Powering ten 100 W light bulbs

To demonstrate the device's ability to supply power to a realistic load, ten 100 W light bulbs were lit using 1 kW power transferred through the 5 mm thick titanium plate. This demonstration was executed by applying a continuous signal to the transmission device at 24.5 kHz for approximately five seconds. In Figure 4, the power amplifiers are on the left, the ten light bulbs in the middle, the transmission device with current probe next to it, and the function generator in the top right. After using the Mat-Lab code designed to compensate for phase errors from the current probe, it was found that the overall transmission efficiency was 84%.

Piezoelectric stacks in the future

This study focused on developing a device capable of transmitting 1 kW of electric power through a metal wall using acoustic stress waves and piezoelectric stacks. Our results show that transmitting power at levels of more than 1kW is feasible using a device that consists of four 38 mm diameter piezoelectric transducer disks. While the overall goal was met successfully, further work must be done before a prototype power transmitter is ready for space applications. Further modeling needs to be conducted to determine the design parameters that will allow for longer, efficient transmission periods and for operation on larger areas. In a final design where acoustic losses become important due to the larger surface area of the device, the energy loss due to the Lamb waves can be reduced with radial reflectors in the wall concentric about the piezoelectric stacks. In addition, the maximum operating temperature of the device needs to be determined for extended transmission periods because the performance characteristics of piezoelectric ceramic rings are temperature sensitive. Finally, other design geometries need to be investigated in order to optimize a design that will maximize the transmission efficiency, reduce the amount of generated heat, and minimize the energy loss due to Lamb waves.

Acknowledgments

Research reported in this manuscript was conducted at the Jet Propulsion Laboratory (JPL), California Institute of Technology, under a contract with National Aeronautics Space Agency (NASA). I would also like to thank Dr. Yoseph Bar-Cohen and the members of his Advanced Technologies Group at JPL, as well as the University of Washington.

Further Reading

Hu Y., X. Zhang, J. Yang, Q. Jiang, "Transmitting Electric Energy Through a Metal Wall by Acoustic Waves Using Piezoelectric Transducers," *IEEE Transactions on Ultrasonics, Ferroelectrics, and Frequency Control*, 50, 7, pp. 773- 781, 2003.



Figure 4. Ten 100W light bulbs powered by the wireless transmission device for ~5 seconds.

Sherrit S., Badescu, M.; Xiaoqi Bao; Bar-Cohen, Y.; Chang, Z., "Efficient electromechanical network model for wireless acoustic-electric feed-throughs," *Proceedings of the SPIE - The International Society for Optical Engineering*, v 5758, n 1, 2005, p 362-372.

Bao X., B. J. Doty, S. Sherrit, M. Badescu, Y. Bar-Cohen, J. Aldrich, and Z. Chang, "Wireless piezoelectric acoustic-electric power feedthru," Paper #6529-134, *SPIE Smart Structures and Materials Symposium*, San Diego, CA, March 19-22, 2007.

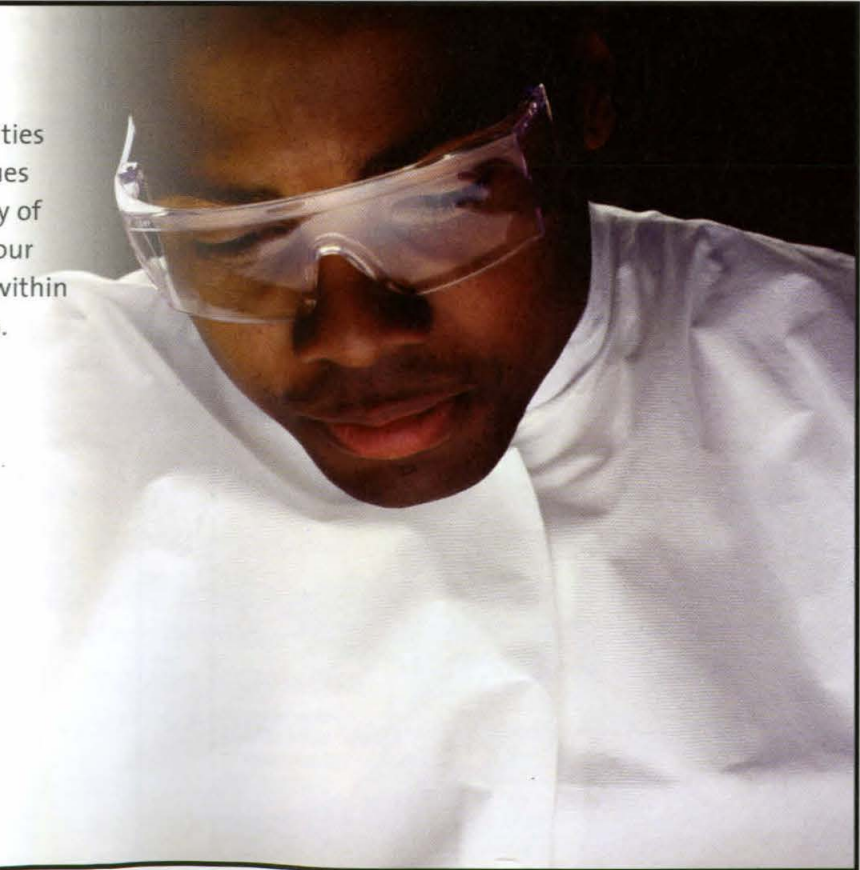
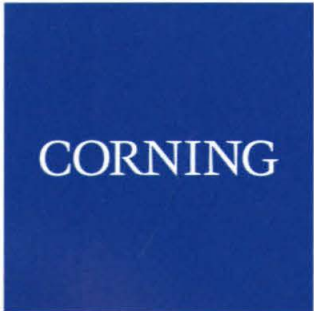
Bar-Cohen Y. B. Doty, S. Sherrit, M. Badescu, X. Bao, J. Aldrich, and Z. Chang, "Power Transmission using Wireless Acousto-Electric Feed-through," *Advanced Concepts and Technology Innovations, and NASA Exploration Systems Research and Technology Program Office, Exploration Systems Mission Directorate, FINAL REPORT*, December 4 2006.

moore ruble yudell

architects & planners

933 PICO BLVD
SANTA MONICA CA
90405
310 450 1400
FAX 310 450 1403
www.mryarchitects.com

At Corning, unparalleled opportunities stem from a commitment to values that are the bedrock of our legacy of innovation. To learn more about our values and career opportunities within Corning, go to www.corning.com.



Institute for Defense Analyses
Studies & Analyses Center, Alexandria VA



Do you have an advanced degree (MS, PhD) in the sciences, engineering, operations research, economics or technology policy and an exceptional knowledge of your technical field?

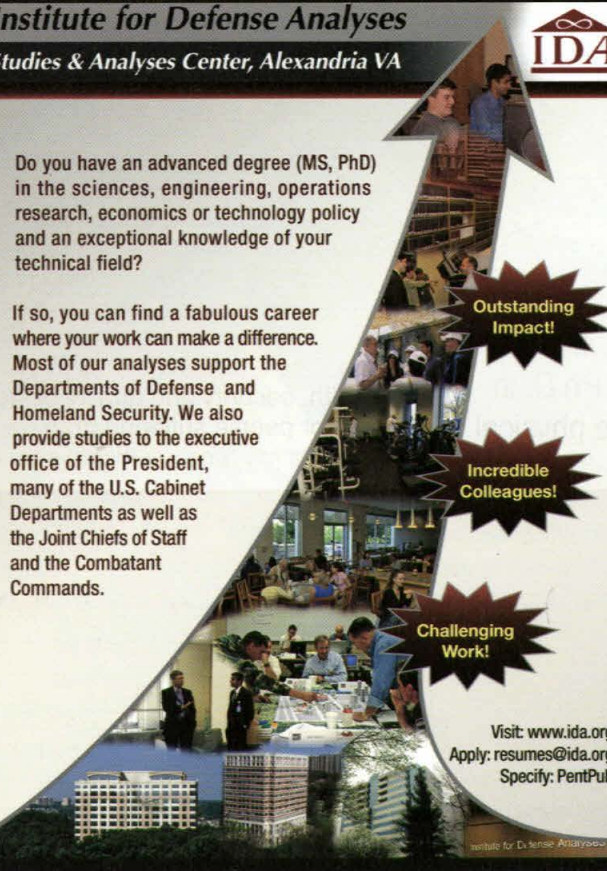
If so, you can find a fabulous career where your work can make a difference. Most of our analyses support the Departments of Defense and Homeland Security. We also provide studies to the executive office of the President, many of the U.S. Cabinet Departments as well as the Joint Chiefs of Staff and the Combatant Commands.

Outstanding Impact!

Incredible Colleagues!

Challenging Work!

Visit: www.ida.org
 Apply: resumes@ida.org
 Specify: PentPub



The Future of Interface Technology



Synaptics is a leading developer of human interface solutions for mobile computing, communications, and entertainment devices.

Synaptics thrives because of its dynamic and diverse employees. We're interested to add intelligent, passionate, adventurous people to our team.



Synaptics™

Join your fellow Alumni!



A career with Cascade Microtech, the world leader in advanced microelectronic probing solutions can provide you with an entirely new way to view success. From our vantage you will benefit from the experience, resources and expertise of an industry leader with an unmatched record of technological "firsts". And from the perspective of our global presence you can leverage your skills and abilities to take advantage of the unprecedented opportunities in this rapidly expanding market.



Toyon's high caliber technical staff supports R&D efforts for the DoD.

We are looking for candidates with B.S, M.S. & Ph.D. in engineering or the physical sciences. Opportunities exist in Santa Barbara, CA or Washington, DC.

- Radar & Optical Sensors
- Algorithm Development
- Modeling and Simulation
- Systems Analysis

For career opportunities:
www.toyon.com



ALFRED MANN FOUNDATION

The Alfred Mann Foundation is a nonprofit medical research foundation, dedicated to bringing advanced medical technologies to the public to provide significant improvements to the health, security and quality of life for people suffering from debilitating medical conditions.

WE CURRENTLY HAVE OPENINGS FOR:

- Sr. Electrical Engineer
- Sr. Test Engineer
- Business Analyst
- Regulatory Affairs Mgr.
- Biomedical Engineer - Mechanical

Visit us at www.aemf.org

Raytheon



The career you'll launch – powerful.
The innovations you'll create – legendary.

When you start a dynamic career with Raytheon, you will join a company that's at the forefront of innovation. Every day 73,000 employees help solve some of the most demanding challenges on the planet. We're looking for passionate, talented individuals to design sophisticated systems and platforms that will redefine multiple industries. Be part of a diverse culture that has been recognized as one of *BusinessWeek* magazine's "Best Places to Launch a Career." Help us build an amazing future with the next generation of technology.

www.rayjobs.com/campus

© 2008 Raytheon Company. All rights reserved. "Customer Success Is Our Mission" is a registered trademark of Raytheon Company. Raytheon is an equal opportunity and affirmative action employer and welcomes a wide diversity of applicants. U.S. citizenship may be required.

Raytheon

Customer Success Is Our Mission